Impact of increased resolution on the representation of the Canary upwelling system in climate models

Adama Sylla [1,2], Emilia Sanchez Gomez[1], Juliette Mignot[3], and Jorge López-Parages[1,4]

[1]CECI, Université de Toulouse, CNRS, CERFACS, Toulouse, France
[2]Laboratoire de Physique de l'Atmosphère et de l'Ocean Simeon Fongang (LPAO-SF/ESP/UCAD), Dakar, Senegal
[3]Sorbonne University (CNRS/IRD/MNHN), LOCEAN Laboratory, Paris, France
[4]Physical Oceanography Group, University of Málaga, Spain.

Correspondence: Adama Sylla (adamasylla36@gmail.com)

Abstract.

We investigate the representation of the Canary upwelling system (CUS) in six global coupled climate models operated at high and standard resolution as part of the High Resolution Model Intercomparison Project (HighResMIP). The models performance in reproducing the observed CUS is assessed in terms of various upwelling indices based on SST, wind stress and sea surface height, focussing on the effect of increasing model spatial resolution. Our analysis shows that possible improvement in upwelling representation due to the increased spatial resolution depends on the sub-domain of CUS considered. Strikingly, along the Iberian Peninsula region, which is the northernmost part of the CUS, the models show lower skill at higher resolution compared to their corresponding lower resolution version in both components for all the indices analyzed in this study. On the contrary, over the southernmost part of the CUS, from the north of Morocco to the Senegalese coast, the high ocean and atmosphere resolution models simulate a more realistic upwelling than the standard resolution models, which largely differ from the range of observational estimates. These results suggest that increasing resolution is not a sufficient condition to obtain a systematic improvement in the simulation of the upwelling phenomena as represented by the indices considered here, and other model improvements notably in terms of the physical parameterizations may also play a role.

1 Introduction

The upwelling is an upward motion of sea water from intermediate depths toward the ocean surface resulting from the friction of the surface wind on the ocean surface. Upwelled water masses are colder and richer in nutrients than the surface waters they replace. Therefore, upwelling zones correspond to areas of very productive marine ecosystems and high fish resources Herbland et al., 1974; Minas et al., 1982; Huyer, 1983 and Tretkoff, 2011). In for areas where the upwelling occurs along the coast, this phenomenon presents a noticeable socio-economic importance or the countries concerned, in particular in relation to the fisheries sector (Gómez-Gesteira et al., 2008). From the physical point of view, coastal upwelling is mainly caused by prevailing trade winds blowing equator-ward parallel to the coastline, which push the surface waters away the coast through the so-called Ekman transport. As a result, the divergent flow at the surface is compensated by an onshore flow from below that brings colder and nutrient-rich waters to the surface. In addition, positive divergent oceanic circulation may also be triggered at

the surface by a cyclonic wind stress curl. Indeed, in the eastern subtropical basins, where trade winds tend to slow down near the coast, the wind drop-off induces a cyclonic wind stress curl that also contributes to upwelling (Pickett, 2003, Capet et al., 2004 and Bravo et al., 2016). This second effect is associated with the so-called Ekman pumping, and it acts to side up deeper waters into the euphotic zone. Both offshore Ekman transport and Ekman pumping contribute to enhance the nutrients levels in leading to an enhanced biological production along the coast (Pennington et al., 2006). There are four major coastal upwelling systems (hereafter EBUSs for Eastern Boundary Upwelling Systems) in the global ocean, that are the Canary, Benguela, Humboldt and California systems. These areas cover less than 1% of the global ocean surface, but they contribute more than 20% of the global fish catches (Pauly and Christensen, 1995).

Among the four EBUSs mentioned above, we focus here on the Canary Upwelling System (CUS), which extends from the northern tip of the Iberian Peninsula at $43°N$ to the south of Senegal at about $10°N$ (Fig.1). The variability of this upwelling system has been studied on seasonal time scale (Torres, 2003 and Alvarez et al., 2005). It has also been studied on longer timescales, but to a lesser extent, due to the lack of sufficiently long, continuous time series (Blanton et al., 1987). In the CUS, the strength of the upwelling favorable winds are associated with latitudinal variation of the Inter-tropical Convergence Zone (ITCZ) and the Azores high pressure system which are both part of the Hadley-circulation. The Azores high pressure migrates from $25°N$ in late winter and $35°N$ in late summer. The Azores High drives both the intensity and the latitudinal extension of the north-easterly winds along the CUS (Wooster et al., 1976; Van Camp et al., 1991; Mittelstaedt, 1991; Nykjær and Van Camp, 1994 and Benazzouz et al., 2014).

According to previous studies, the CUS can be divided into different sub-systems based on its circulation, physical environment and shelf dynamics (Santos et al., 2005; Gómez-Gesteira et al., 2008 and Arístegui et al., 2009). The western coast of the Iberian Peninsula located between $37°N$ to $43°N$ (hereinafter IP), is the northern limit of the CUS. The IP presents a discontinuity in the flow with the northwest African coast (Arístegui et al., 2004). This is caused by the presence of the Strait of Gibraltar, which allows the exchange of water between the Mediterranean Sea and the Atlantic Ocean. Upwelling activity along the western coast of the IP occurs during boreal summer due to the poleward migration of the Azores high, which leads to northerly winds flowing along the coast (Wooster et al., 1976; Fraga, 1981; Blanton et al., 1984; Bakun and Nelson, 1991; Gomez-Gesteira et al., 2006; deCastro et al., 2008a; Alvarez et al., 2008 and Pires et al., 2013). Furthermore, the narrow shelves of IP coast result in lower annual biological productivity than in the other sub-regions of the CUS (Arístegui et al., 2009). In the area surrounding the Gibraltar Strait (from latitude $33°N$ to $36°N$), the upwelling is drastically reduced.

The Morocco upwelling system (hereinafter MoUS), located form $21°N$ to $32°N$ is the central part of the CUS. According to several studies the MoUS can be divided into two sub-domains: the northern part (nMoUS) and the southern part (sMoUS), extending between $26°N$-$32°N$ and $21°N$-$25°N$ respectively (Santos et al., 2005; Gómez-Gesteira et al., 2008 and Arístegui et al., 2009). In the nMoUS, upwelling occurs during the boreal summer, while the sMoUS is one of the few locations in the world where upwelling is persistent throughout the year. This permanent upwelling is due to the fact that, unlike in the

case of the other sub-regions within CUS, in sMoUS the prevailing winds are always parallel to the coastal line and blowing equatorward.

Finally, in the southern part of CUS, the Senegalo-Mauritanian Upwelling System (SMUS), which extends from 12°N to 20°N is the southernmost part of the CUS. Here the upwelling occurs from November to May, when the ITCZ reaches its southernmost position (Faye et al., 2015 and Sylla et al., 2019).

In the last decades, the sensitivity of EBUSs to climate change has received increasing attention (Bakun, 1990; McGregor et al., 2007 and Barton et al., 2013). Improving our knowledge of the response of the CUS to global warming is of crucial importance since the food resources and economy of neighbors countries greatly depends on its characteristics and evolution in the coming decades. By using the averages of the meridional wind stress component derived from ship reports, Bakun (1990) suggested that coastal upwelling intensification would occur in response to continued global warming. Specifically, he argued that anthropogenic climate change air temperatures on the continents are expected to rise more than in the adjacent oceans (Manabe et al., 1991), producing a deepening of the thermal low-pressure systems over land which lead to an intensification of the land-sea sea level pressure gradients, and a subsequent increase of summertime upwelling-favorable winds (Rykaczewski et al., 2015). Efforts to test Bakun's hypothesis of upwelling intensification under the recent warming trend are challenged by the limited spatial and temporal extent of observations (Cardone et al., 1990). In this context, climate models offer an alternative method to simulate large-scale representation of the CUS and its sensitivity to increased greenhouse gas concentration. By using upwelling indices based on wind-stress and/or sea surface temperatures (SSTs), Wang et al. (2015) and Sylla et al. (2019) show that climate models, as those participating within the Coupled Model Intercomparison Phase (CMIP) exercises, are able to capture the main characteristics of the EBUSs. According to Pickett (2003), the success of these low-resolution estimates of coastal upwelling may depend on their implicit integration of both near-shore Ekman transport and offshore Ekman pumping. Nevertheless, standard resolution global climate models suffer from several limitations as they do not represent finer scale processes associated with the upwelling, in particular the structure of the offshore wind-stress divergence and curl (Small et al., 2015 and Vazquez et al., 2019 and references therein). Indeed, most coupled climate models incorrectly simulate various processes occurring in these regions and suffer from warm SST biases (Richter, 2015). Misrepresentation of stratocumulus clouds has been identified as one of the primary reasons for this bias. Model inability to produce stratocumulus decks can lead to absorption of excessive shortwave radiation in the upper-ocean and anomalously warm SSTs, which in turn induces a positive feedback to the initial error (Richter, 2015 and Zuidema et al., 2016). Further, model resolution and errors in surface winds could also play a role through their impact on turbulent fluxes, coastal upwelling and offshore Ekman transport (Gent et al., 2010; Richter, 2015; Zuidema et al., 2016 and Ma et al., 2019). Most coupled climate models suffer from warm biaises, in SST and wind, near the subtropical eastern boundary regions (Davey et al., 2002; Richter and Xie, 2008 and Richter et al., 2012). Despite numerous improvements in models over time, these problems have persisted because of their coarser resolution. However increasing model resolution leads to an improvement of the upwelling representation, in particular the SST warm biases over the upwelling regions are reduced (Small et al., 2015). Some works have concluded that model resolution influences on the the overall representation of the mean climate over the Tropical Atlantic (Doi et al., 2012 and Exarchou et al., 2018)

and on the tropical north Atlantic response to remote forcings such as ENSO (López-Parages and Terray, 2022). In line with these studies, Gent et al. (2010) report that an increase of the nominal resolution of the atmospheric grid from $2°$ to $0.5°$ lowers SST biases up to 60% within the major upwelling areas. Harlass et al. (2015) found that a significant improvement of warm biases within the Tropical Atlantic can be reached with a simultaneous refinement of the horizontal and vertical resolutions of the atmospheric grid. Small et al. (2015) claimed that a good representation of the upwelling systems as the Benguela (coastal upwelling along the southern African coast) requires an eddy-resolving ocean model and an atmospheric model with enough resolution ($\sim 0.5°$) to capture realistically the wind stress curl over the eastern boundary of the Tropical Atlantic Ocean.

Thus in the last few years, modelling centers have made a great effort to develop higher resolution global climate models. The recent CMIP6 exercise coordinated the High Resolution Model Inter-comparison Project (HighResMIP/PRIMAVERA), aiming to assess the benefits of increased resolution in climate models (Haarsma et al., 2016). Climate models resolution was drastically increased in the atmospheric and oceanic components and for the first time a coordinated protocol was proposed to asses the impact of enhanced model resolution in the representation of the climate system. This is a topic of growing interest, particularly as some recent simulations suggest improvements in both large-scale aspects of the atmospheric and ocean circulation and in small-scale processes and climate extremes (Haarsma et al., 2016; Roberts et al., 2016; Vanniere et al., 2019 and Hewitt et al., 2020). So far, the effects of increased CMIP6 model resolution on the upwelling systems has still not been assessed. Here, we provide the first detailed analysis of the potential benefits of increasing model resolution in simulating the CUS. To this aim, we compare the model performance in representing the upwelling indices defined in Sylla et al. (2019) by using the standard and high resolution versions of some of the climate models that participated within the CMIP6 HighResMIP project. The upwelling indices used in this study are based on SST and wind stress. The SST index aims at describing the surface thermal signature of the CUS upwelling. Although this is a simplified view of the upwelling, this index has the advantage of being based on a well-observed variable so that it can be properly constrained by observations. The other three indices used here are based on the surface wind stress and meridional gradients of sea level. They aim at quantifying key mechanisms implicated in the generation of upwelling vertical velocities: coastal divergence of the Ekman transport, Ekman pumping, and possible counteracting effects due to convergences of the geostrophic flow.

The manuscript is organized as follows: Section 2 describes the numerical experiments, the observational and reanalyses datasets as well as the different metrics used in this study. Section 3 provides a characterization of the upwelling in observations, while the role of the model resolution in simulating the CUS is assessed in Section 4. Finally, results are discussed and a conclusion is provided in section 5.

2 Data and methodology

2.1 Models and numerical experiments

The coupled models considered in this work are those participating in the European H2020 HighResMIP/PRIMAVERA project (https://www.primavera-h2020.eu) which is part of the international HighResMIP exercise. We use the outputs of coupled historical experiments (referred to as 'hist-1950') covering the period 1950-2014. In particular, the models used are HadGEM3 GC3.1 (Williams et al., 2018), CNRM-CM6-1 (Voldoire et al., 2019), CMCC-CM2 (Cherchi et al. 2019), MPI- ESM1 (Gutjahr et al., 2019), ECMWF-IFS (Roberts et al., 2018), and EC-Earth3P (Haarsma et al., 2020). The main characteristics of these models are listed in Table 1 together with the respective effective resolutions in both the atmosphere and ocean components. Note that for the PRIMAVERA coordinated project, resolution was increased in both the atmosphere and the ocean components, with the exception of CMCC-CM2 and MPI-ESM1, in which only the atmospheric resolution was modified. Based on the change of ocean and/or atmosphere resolution four groups of models are defined: groups 1 and 1* including low resolution models (LR), and groups 2 and 2* including high resolution models (HR) for both the atmosphere and the ocean. From group 1 to group 2, both the ocean and the atmosphere resolution is increased. From group 1* to group 2*, only the atmosphere resolution is increased. Note that our set of model is an ensemble which does not allow a precise comparison of the effect of increasing both ocean and atmosphere resolution on the one hand (groups 1-2), or only increasing the atmosphere resolution on the other hand (1*-2*). Indeed, the resultant model groups do not contain the same models and are not of the same side. Thus, some of the differences among the ensembles of model groups may be due to the intrinsic models biases rather than an effect of model resolution. This drawback has to be kept in mind. Furthermore "standard" and "high resolution" terms are rather subjective and depend on the context. Here, we use them in the context of global climate modelling, so that standard resolution is around $1°$ for the ocean, and high-resolution around $0.25°$. We acknowledge that the high-resolution ocean models in this study can barely resolve the first baroclinic Rossby radius deformation (20-60 km, Chelton et al 1998) in most parts of the CUS. Similarly, the standard atmospheric resolution is $1°$ to $2.5°$ while most of the high-resolution atmospheric components in this study are about $0.5°$ which may not be able to resolve realistic wind structure/drop-off near the coast (Patricola and Chang, 2017). So, even models described here as "high-resolution" can probably realistically not resolve upwelling dynamics in this region, at least not as well as dedicated configurations (for example ROMS numerical simulation including a high resolution grid $1/60°$ ($\sim$2 km) and a standard resolution $1/12°$ ($\sim$10 km) ; e.g: Ndoye et al., 2017).

Our analysis is based on the SST wind stress, sea surface height and mixed layer depth monthly fields (see section 2.3). For each variable we compute the 30 years climatological mean for the period 1985-2014. The choice of this period is motivated by the selection of a common period among the various observational datasets used in this study. To avoid biased multi-model ensemble means, only one member of each model was used even if several members are available for certain models. Note that the different members have been averaged together in order to increase robustness of the seasonal cycle estimation, nevertheless the results does not change (not shown). Additionally, the choice can be also justified by the fact that our metrics are based on climatological averages and not on variance or trends metrics, which are more sensitive to internal climate variability.

2.2 Observational and reanalyses products

Several observational and reanalysis datasets are used in the present analysis (see Table 2 for details) in order to evaluate model results realism in simulating the CUS. For SST, we use the monthly HadISST.2 dataset, which was developed at the Met Office Hadley Centre for Climate Prediction and Research (Titchner and Rayner, 2014) We have also used the version 2 of the National Oceanic and Atmospheric Administration (NOAA) Optimum Interpolation Sea Surface Temperature (OISST-v2) analysis (Reynolds et al., 2007). The OISST analysis combines Advanced Very High Resolution Radiometer (AVHRR) satellite data, buoy and ship-based observations from the International Comprehensive Ocean Atmosphere Data Set (ICOADS) database (Worley et al., 2005) . Although these data are provided with at daily frequency, monthly averages have been computed. Finally, we have also included the latest version of the Extended Reconstructed Sea Surface Temperature data set (ERSST-v5, Huang et al., 2017). The monthly ERSST-v5, produced by the National Oceanic and Atmospheric Administration (NOAA), is based on in situ (ship and buoy) observations from ICOADS.

The Quikscat wind speed and the zonal and meridional components of the 10-m wind from the Cross-Calibrated Multi-Platform (CCMP) project are also analyzed (Freilich and Spencer, 1994; Atlas et al., 2011). In addition to the observational products, near surface wind data from two atmospheric reanalysis have been considered and compared to the previous observational winds products using a wind rose diagram (Fig A1 in Appendix A): the latest climate reanalysis ERA5, provided by the European Centre for Medium-Range Weather Forecasts (ECMWF; Hersbach et al., 2020). The latter is supported by the version 3 of the NOAA-CIRES-DOE 20th Century Reanalysis (20CRv3) Project (Slivinski et al., 2019). The NOAA-20CR-v3 datasets are supported by the National Oceanic and Atmospheric Administration (NOAA), the Cooperative Institute for Research in Environmental Sciences (CIRES), and the U.S. Department of Energy.

Because of a lack of wind stress observations and reanalysis covering the entire domain and period of our study (1985-2014), the surface wind speed is converted into wind stress following an empirical method (see Appendix A for more details). Note that this offline computation of the wind stress is only performed for the observations and reanalyses wind datasets but not for the model, which directly provides the wind stress field.

Meridional sea surface height (SSH) gradients may also play an important dynamical role in coastal regions through geostrophic transport (Marchesiello and Estrade, 2010). Cross-shore geostrophic transport can substantially alter the vertical transport relative to wind-based estimates (Rossi et al., 2013 and Jacox et al., 2014). Thus including the geostrophic component is also important to assess the realism of the modeled upwelling (Rykaczewski et al., 2015 and Oerder et al., 2015). To evaluate the models representation of SSH along the CUS, we use the AVISO satellite altimetry product (Ducet et al., 2000). For comparison, we have also used the monthly mean SSH from GODAS. Furthermore, to quantify the effect of the SSH gradient on the geostrophic transport requires an estimation of the oceanic mixed layer depth (MLD). We use the MLD climatology from de Boyer Montégut, 2004. This MLD climatology is based on ARGO profiles where MLD was estimated following a density criterion at a monthly resolution. The selected criterion is a threshold value of temperature (namely $0.2°C$) from a near-surface

value at 10 m depth.

Monthly climatologies over the 1985-2014 period are considered for all the validation datasets and models as specified in section 2.1, except for CCMP and AVISO, which are both based on a shorter time period (1992-2011 and 1995-2005 respectively).

2.3   Upwelling indices

195   We compute the upwelling indices developed in Sylla et al. (2019) for the SMUS and applied here to the whole CUS. The relevance of these indices to represent CUS variability is justified in section 3. We consider the SST difference between the coast (black dots all region, Fig. 1) and the outer ocean (magenta dots, Fig. 1) in such a way that the SST-based index is defined by:

$$UI^{sst} = SST_{ocean} - SST_{coast} \tag{1}$$

200   Typically a distance of $5°$ longitude from the coast is considered for this index (Cropper et al., 2014 and Sylla et al., 2019). This SST upwelling index has been widely used to characterize upwelling intensity as it measures the impact of upwelling on the SST zonal structure (Mittelstaedt, 1991; Santos et al., 2005; Gómez-Gesteira et al., 2008; Lathuilière et al., 2008 and Marcello et al., 2011). Positive (negative) values of the index correspond to more intense upwelling (downwelling).

205   As described in the introduction section, the influence of wind on the upwelling can be separated into two mechanisms (Sverdrup et al., 1942; Yoshida, 1995 and Smith, 1968). The first mechanism, called the Cross-Shore Ekman Transport (hereafter $CSET$) is commonly used for characterizing coastal upwelling (Bakun, 1973; Schwing et al., 1996 and Gómez-Gesteira et al., 2008). $CSET$ is computed as the offshore component of Ekman transport (Q), whose zonal and meridional components are derived from the wind stress field as follows:

210   $$Q_x = \frac{\tau_y}{\rho_w f} \quad and \quad Q_y = -\frac{\tau_x}{\rho_w f} \tag{2}$$

where ρ_w is the sea water density (1025 kg.m^{-3}) and f is the Coriolis parameter. Following Santos et al. (2012), the zonal and meridional components of the Ekman transport are used to calculate $CSET$ from a discrete set of points parallel to the shoreline (Fig. 1, black dots):

$$CSET = -\sin(\phi)Q_x + \cos(\phi)Q_y \tag{3}$$

215   where $CSET$ is expressed in $m^2 s^{-1}$ and ϕ represents the angle between the shoreline and the equator. Whilst presenting a highly irregular topography, the coastline within CUS can be broadly approximated to $90°$ over IP, to $55°$ over MoUS and to $90°$ off the SMUS coast relative to the equator (Alvarez et al., 2008 and Cropper et al., 2014). Positive (negative) values of $CSET$ correspond to upwelling-favorable (unfavorable) conditions.

The second mechanism contributing to upwelling is the Ekman pumping (W_{ek}) defined as:

220   $$W_{ek} = \frac{1}{\rho_w f} \int_{long} \nabla \times \tau \tag{4}$$

where W_{ek} is expressed in $m^2 s^{-1}$, $\int_{long} \nabla \times \tau$ represents the curl of the derived wind stress vector integrated over the longitude range of IP, nMoUS, sMoUS and SMUS subregions (different boxes in Fig. 1).

Finally, as highlighted in section 2.2, coastal upwelling may be modulated by the cross-shore geostrophic transport. We quantify this effect along the CUS subregions as follows:

$$T_{geo} = MLD \frac{g}{f}(SSH_{north} - SSH_{south}) \tag{5}$$

where T_{geo} is the vertical transport (in Sv) due to the zonal current generated from the meridional SSH gradient and g is the gravity coefficient (g = 9.81 m.s^{-2}). T_{geo} is calculated right next to the coastal boundary, where it can interact with the vertical flux. Thus SSH_{north} - SSH_{south} is the difference between the northernmost and southernmost grid point close to the shore of the different sub-regions of the CUS (see Fig. 1). In addition, the MLD is averaged over each box marked in Fig. 1 (IP, nMoUS, sMoUS and SMUS subregions). Note that all indices described above are calculated over the native model grid. However, the metric used here (see section 2.4) to evaluate the models skill requires an interpolation. For this and only for the skill calculation (Fig.6) all the models have been interpolated from their native grids to a common 0.25°x0.25° lat-lon resolution grid, using a bilinear interpolation method. We noted that small changes are induced by the interpolation method (not shown) but this does not affect the skill scores in a statistically significant way.

2.4 Skill metrics

We use a metric to quantify the skill of the climate models at representing the CUS characteristics through the different upwelling indices. In this study we use the Arcsi-Mielke score (M) previously used to evaluate the performance of High-ResMIP/PRIMAVERA model (Bador et al., 2020).
This is a non dimensional metric defined by:

$$M = (\frac{2}{\pi})\arcsin\left[1 - \frac{mse}{V_X + V_Y + (G_X - G_Y)^2}\right] \times 1000 \tag{6}$$

where mse is the mean-square error, X and Y represent model and observed data respectively, V is the spatial variance and G the spatial mean. The Arcsin-Mielke score reaches a maximum possible value of 1000 when mse is equal to 0, whereas a zero score indicates no skill and it can even be negative in the worst cases, although this rarely occurs. The skill score is computed separately over the different subdomains of the CUS and for the annual climatological averages of each upwelling index. To compute M all the upwelling indices have been interpolated on a common 0.25°x0.25° horizontal grid by using a bilinear interpolation method.

3 Characterization of the Canary upwelling system from observations and reanalysis

In this section, we describe the upwelling indices defined above computed for the observation datasets. These indices are shown in Fig 2, Fig.3, Fig.4 and Fig.5 for both the data and models but only the observations panels are described here. The results from the modelling experiments will be described in section 4.

3.1 The thermal upwelling indices

The seasonal variability of the CUS upwelling intensity as described by the UI^{sst} index is shown in Fig. 2 (left panels) in the observations and reanalysis. Over the IP coast, the strongest positive values of UI^{sst} are observed in summertime (July to September) and the index remains positive but weaker ($0.5°C$) from November to June. This evolution is consistent with the available literature (Nykjær and Van Camp, 1994; Santos et al., 2005 and deCastro et al., 2008b). The ocean-coast gradient (i.e., the UI^{sst} index) ranges from $1°C$ to $4°C$ from lat $21°N$ to $32°N$ (MoUS), with high values of UI^{sst} through the whole year in sMoUS and during summer time (July to September) in nMoUS. The presence of the above mentioned high values of UI^{sst} throughout the year in sMoUS are consistent with the permanent upwelling conditions described in previous works (Wooster et al., 1976; Barton et al., 1998 and Gómez-Gesteira et al., 2008). Further south, over the SMUS region, UI^{sst} shows a marked seasonality with positive values of UI^{sst} in winter (upwelling season) and negative values of UI^{sst} in summer.

Fig. 2 reveals that although the three observational datasets present a similar behavior of UI^{sst}, substantial differences in the amplitude emerge. The largest discrepancies are found in sMoUS (whole year) and SMUS (winter) where UI^{sst}, values are significantly lower in ERSST-v5 than in the other datasets. In the rest of CUS subregions (i.e., IP and nMoUS), a stronger observational agreement is found.

3.2 Dynamical upwelling indices

Fig. 3 shows the seasonal cycle of $CSET$ for observations and reanalysis (left panels). Along the western coast of the IP, upwelling-favorable conditions (positive values of $CSET$) are observed during summer. This is coherent with the strengthening and northward displacement of the Azores high which promotes northerly winds. This marked upwelling season in summer is consistent with the results obtained from the thermal index (UI^{sst}) and with the previous research (Alvarez et al., 2005; Santos et al., 2005 and Gomez-Gesteira et al., 2006). As for UI^{sst} (Fig. 2), negligible or even negative values of $CSET$ are detected along the IP coast during wintertime indicating the predominance of downwelling conditions.

Also consistent with previous studies (Gomez-Gesteira et al., 2006 and Benazzouz et al., 2014), $CSET$ is strong in summer in nMoUS and permanent throughout the year in sMoUS. Finally, the SMUS is characterized by the existence of two well marked seasons: an upwelling season from approximately November to May and a downwelling season from June to October.

As for SST, the comparison between wind products also shows some discrepancies in terms of upwelling amplitude. Despite the CCMP wind dataset covers a shorter time period (1992-2011), there is no major difference with respect to ERA5. On the contrary, NOAA-20CR-v3 shows a slight enhance $CSET$ with respect to the other two datasets, particularly for SMUS and nMoUS from April to June. A conclusion emerging from this analysis is that the Ekman transport might therefore depend on the underlying size of the grid cell. Thus, gridded datasets at different resolutions may lead to different estimates of the observed Ekman transport. This sensitivity of the Ekman transport to the spatial resolution is therefore crucial to properly compare modeled and observed upwellings.

Fig. 4 shows the seasonal cycle of the Ekman pumping (W_{ek}). Focusing on the validation datasets (left panels) and over the IP, W_{ek} tends to be weak or practically zero from October to June, and it is more intense (around 0.5 $m^2 s^{-1}$) during summer season in CCMP and ERA5 as found by Alvarez et al. (2008). For NOAA-20CR-v3, this seasonal cycle is less marked. Along the MoUS, W_{ek} is different in nMoUS and sMoUS sub-regions. In sMoUS, W_{ek} is weak but positive with maximum values occurring during winter and spring. In nMoUS, validation datasets show mostly negative values of W_{ek} throughout the year as found by Lathuilière et al. (2008). This result may be linked by the fact that the meridional component of the wind stress (V) decreases (instead of increases) away from the coast. This results in negative $\frac{\partial V}{\partial x}$ in this region (not show) and favorable conditions for downwelling. Finally along the SMUS W_{ek} is maximum in winter and spring. Therefore, the seasonal cycle of W_{ek} is roughly that for $CSET$ (Fig. 3), with the main differences identified over the MoUS.

3.3 The onshore geostrophic flow and the quantitative assessment of the upwelling rate

As discussed in section 2, the effect of T_{geo} is quantified here for the CUS. We have examined firstly the monthly climatology of the meridional sea surface height gradient from the AVISO satellite data and the GODAS reanalysis (see first two columns in Figure B1 of the appendix B). The SSH gradient observed over IP (panel a) is indeed negative all the year, thus potentially inducing an onshore geostrophic flow. The maximum and minimum amplitudes of this SSH gradient are found in summer and winter, respectively. Over MoUS (panels b and c), this gradient is negative all the year as for the IP and reach its maximum from May to November in the nMoUS and from July to September (August to October) over sMoUS in AVISO (GODAS). In the SMUS (Fig B1, panel d) the SSH difference is also always negative and the related amplitude strongly differs from the others subregions (IP, nMoUS and sMoUS). Therefore, these SSH meridional gradients yield to an onshore geostrophic transport (T_{geo}) off the CUS during the upwelling season. It is important to mention that the latter term (T_{geo}) is counted negative eastward following the sign convention used to quantify the upwelling (negative bars in Fig.5). The T_{geo} is below 0.25 Sv over IP (Fig.5a) in the three validation datasets. For nMoUS (Fig.5b) and sMoUS (Fig.5c) subregions, T_{geo} is on average $\sim$0.25 Sv. Finally, the contribution of T_{geo} is strongest over the SMUS, which presents values of 0.6 Sv approximatively. This situation is mainly related to the fact that this subregion shows stronger SSH gradients than the rest of the CUS (panel d, Figure B1).

The physical and biogeochemical responses to coastal divergence and Ekman suction differ in important ways (Capet et al., 2004 and Renault et al., 2016). As a first approach, the $CSET$ and W_{ek} may nevertheless be added up to provide an estimate of upwelling strength. Jacox et al., 2018 have recently suggested that the effect of Ekman processes should be estimated globally from the integration of Ekman transport along the boundaries (north, west, and south) of the region of interest. Comparison of this approach with the one proposed here had been performed with CMIP5 (Sylla et al., 2019). This comparison shows that both methodologies in general yield very similar results. In the validation data sets, the difference is less than 5 %, with the Jacox's et al. (2018) approach leading to slightly stronger results, while the multimodel mean is weakened by approximately 10%. Given the similarity of these results, and the interest, in our view, to discuss the open ocean wind stress curl separately from the offshore transport divergence, we consider that the overlap is weak and decide to estimate the total upwelling intensity (UI_{total}) as a sum of the integrated Ekman transport ($CSET$), the Ekman pumping (W_{ek}) and the geostrophic flow T_{geo}.

Furthermore, the comparison of this indirect estimate to a more direct estimate from vertical velocities was also done in Sylla et al., 2019 for CMIP5. The authors show that UI_{total} is consistent with a direct estimation of the upwelling flux from vertical velocities diagnosed from the models.

Fig.5a (green bars) shows that, UI_{total} over IP is positive and ranges between 0.25 Sv and 0.45 Sv. UI_{total} estimation leads to an total upwelling transport of 0.25 Sv to 0.5 Sv over nMoUS (Fig.5b) while it ranges from 0.5 Sv to 1 Sv over sMoUS (Fig.5c). Note that our previous analysis of Ekman pumping (Fig.4) has shown negative values during the upwelling season (summer) in the nMoUS favoring the predominance of downwelling conditions. The combination of both W_{ek} and T_{geo} may thus contribute to reduce the volume of upwelled waters due to the $CSET$ in this subregion. In the SMUS (Fig.5d), where the Ekman divergence and the wind stress curl generate a significant vertical transport proceeds (Fig.3 and Fig.4), our estimation of UI_{total} is about 1 Sv to 1.5 Sv. This upwelling is however partially reduced (as in Sylla et al., 2019) by the strong effect of onshore transport.

4   Models evaluation

4.1   The thermal upwelling indices

To address the models analysis, we compare UI^{sst} from the observational datasets (Fig.2; left panels) and the different model configurations (Fig.2; right panels). In the IP, there is a general agreement between observations and models. Models broadly reproduce the climatological seasonal cycle obtained in observations with a maximum in summer. One exception can be noted: the CNRM-CM6 family shows no signature of upwelling with unrealistic negative values of UI^{sst} during summer. In general, the amplitude of the seasonal cycle is slightly enhanced when both the ocean and atmosphere resolution are increased (comparison among groups 1 and 2).

Along the nMoUS and sMoUS, the group 2 provides a more realistic representation of this SST index than their LR versions (group 1). In the latter case the amplitude is markedly underestimated over the sMoUS subregion. For both groups 1* and 2*, the upwelling is broadly reproduced in these subregions, with an overestimation of UI^{sst} amplitude in MPI-ESM1 over the sMoUS. Thus, the only increase of the atmospheric resolution in models produces no clear impact on upwelling representation. Along the SMUS sub-region and for the group 1 (i.e., the LR model versions), the upwelling season seems to be longer that the observed: it starts earlier (October) and ends later (June), with a marked drop for CMCC-CM2 (group 1*). However both, MPI-ESM1-2-HR and MPI-ESM1-2-XR, simulate a realistic seasonal cycle in comparison with the observations, but the corresponding amplitudes are largely overestimated over the sMoUS and the SMUS. This situation may can be explain by the results found in Gutjahr et al. (2019). According to these authors the MPI model suffers a severe cold bias in the whole northern hemisphere and, particularly, in the Atlantic sector. In this line, Roberts et al. (2019) show that a higher-resolution atmosphere tends to produce a cooler ocean SST, particularly in the ocean upwelling regions (in agreement with Gent et al., 2010 and Small et al., 2014). This cooling has been already assessed by Putrasahan et al. (2019) and is caused by a slowed AMOC due to the underestimation of the wind stress, the northward heat, and the salt transport. The above mentioned deficiencies in the representation of the seasonal cycle seem to be improved when both the atmospheric and the ocean resolution increase (group

2). On the contrary, when just the atmospheric resolution is increased they persist (group 2*).

In summary, increasing the horizontal resolution of the atmosphere or both, the atmosphere and the ocean, alters the representation of the CUS if it is characterized with the thermal index UI^{sst}. Nevertheless, different features are identified along the distinct sub-regions within the CUS. Thus, the IP does not seem to be very sensitive to these changes in model resolution. On the contrary, upwelling representation in the western African coast (MoUS and SMUS) improves when ocean and atmospheric resolution enhance. This is consistent with Ma et al. (2019) and Balaguru et al. (2021) who found that an increase in horizontal resolution can potentially reduce the warm bias of climate models along these regions through an improved simulation of coastal upwelling. This responds to the fact that thermocline rises more sharply near the coast causing a reduction of the near-shore SST bias in the high-resolution global climate models. On the other hand, the comparison of group 1* and group 2* indicates that the upwelling estimated with UI^{sst} does not change significantly when only the atmospheric resolution is increased. Therefore, we infer that enhancing ocean resolution is required to improve the SST-related upwelling index representation over the CUS. This is in agreement with previous studies such as Small et al., 2015 for the Benguela upwelling system. Additionally, Gutjahr et al. (2019) suggest that a high spatial resolution in the ocean reduces the bias in both, the ocean interior and the atmosphere. All this leads to the important conclusion that a high-resolution ocean plays a key role for properly representing the ocean and atmosphere mean states.

4.2 Dynamical upwelling indices

As for the thermal index UI^{sst}, we evaluate the ability of the different model configurations to reproduce the seasonal variability of $CSET$ (Fig.3) and W_{ek} (Fig.4). Along the IP coast all model configurations show the seasonal of $CSET$ with the maximum during summer. However in group 1, the upwelling period is in general overestimated, which is not the case of group 2. Regarding groups 1* and 2*, no major difference has been identified, which therefore difficult to extract a relationship with confidence.

Focusing on the sMoUS and nMoUS, group 1 largely overestimates $CSET$, whereas this overestimation is less well clear for group 1* (Fig.3). On the contrary, group 2 is broadly coherent with the observations and the group 2 * also provides more realistic $CSET$ values than group 1*. This suggest that higher resolution winds lead to an improved Ekman transport. Similar conclusions are generally drawn over the SMUS region for groups 1* and 2* whereas the group 2 shows a better agreement with the validation datasets than group 1. The latter again overestimates the amplitude of the Ekman transport with respect to the reference values. This situation has also been documented in Castaño Tierno (2020).

We consider now the ability of the different model configurations to reproduce the seasonal variability of the wind stress curl (Fig.4). The models reveal sometimes noisy patterns, making complex in these cases the interpretation of the effect of model resolution, but some conclusions can be drawn. Group 2 reproduces the expected larger features of the W_{ek} seasonal cycle in the different subregions, and a comparison with group 1 reveals differences in structure and intensity particularly over the southern flank (MoUS and SMUS). Group 1 shows generally a rather sharp and unrealistic seasonal cycle in SMUS which is longer than that identified in the validation datasets. The improvement in group 2 may be linked to that found by Ma et al.

385 (2019): a finer horizontal resolution of climate models enables better representation of low-level coastal jet structure, with stronger and closer alongshore wind stress and curl leading to a more realistic representation of upwelling. The refinement of just the atmospheric resolution (group 2*) also leads to an improved wind stress curl.

4.3 Geostrophic flow and total upwelling transport

Fig.5 shows the total upwelling transport (UI_{total}) by taking into account the different upwelling terms: $CSET$, W_{ek} and
390 T_{geo}. The latter (computed as described in section 2. 3 and represented in Fig.5 with negative bars) is too weak in group 1 over the IP coast, which is related to the low contribution of SSH gradient in these models during the upwelling season (Fig B1 in Appendix B). When both the ocean and atmosphere resolution are increased (group 2), the realism of T_{geo} is improved. It is broadly consistent with the observational estimates. The CMCC-CM2 family in group 1* and 2* provides realistic T_{geo} values independently of the model resolution. However, this onshore transport is very low (close to zero) in MPI-ESM1 mod-
395 els for both resolutions particularly due to the shallower mixed layer depth (not shown) over the North Atlantic. This feature is consistent with Gutjahr et al. (2019). The effect of increasing only the atmospheric resolution is, therefore, difficult to be established. As in group 1 this is probably due to the relatively weak effect associated with the SSH-related contribution. In nMoUS and sMoUS (Fig.5 panels b and c), the role of the resolution on the simulated T_{geo} is not clear and the difference amongst the groups is very small. Finally in the SMUS region, the more realistic estimates of T_{geo} are generally provided by
400 the group 2 as also the simulated SSH gradient (Fig B1). For groups 1* and 2*, the MPI-ESM1 models show better agreement with observations than the CMCC-CM2 models, but the impact of the atmospheric resolution is again not conclusive.

We consider now the total upwelling transport (UI_{total}) computed as the sum of all dynamical effects, as explained in section 3.2. We find, along the IP coast (Fig.5, panel a), that both groups 1 and 1* markedly overestimate the upwelling total transport.
405 This overestimation is reduced in group 2 with UI_{total} values slightly higher than the observational range (horizontal dashed lines). However minor differences are found among groups 1* and 2 *.
In the nMoUs, the group 1 and group 1* again largely overestimate the total upwelling transport except for the CNRM-CM6-1-LR which shows values almost close to zero and CMCC-CM2-HR4 which provides a generally good estimation of UI_{total}. The very weak value in CNRM-CM6-1-LR can be explained by the downwelling effect displayed by the W_{ek}, which is relatively
410 strong in this model configuration (Fig.4). On average, the HR model versions (group 2) perform better the UI_{total}, which appears within the range of observational estimates. Models of group 2 are generally in the range of observational estimates and the group 2* shows a small improvement with increased resolution. The CMCC-CM2-VHR4 is close to the validation datasets as its LR version, while MPI-ESM1 overestimate always UI_{total}, although the value is smaller in the HR version than in the LR version.
415 In the sMoUS subregion the differences among models resolution are less marked than in the previous regions. Thus, it is difficult to directly relate the representation of UI_{total} with model resolution. Finally over the SMUS domain and as it is seen in Fig.5 panel d, the group 2 have a general better agreement with the observations than the group 1, for which UI_{total} is clearly outside the range of the observed UI_{total}. Thus, models in the group 2 are able to fully capture the estimation of the

upwelling transport by realistically representing all the dynamical indices in such a way that the simulated upwelling in this subregion tend to be systematically more tightly clustered. Groups 1* and 2* show similar range of UI_{total} and no clear effects due to the increasing resolution are identified.

4.4 Quantitative measure of the model skill

In this section, we evaluate quantitatively the performance of the models in simulating the CUS using the Arcsin-Mielke M score (see section 2.4). M is computed between the observed and the simulated upwelling indices as a function of the nominal ocean resolution. The reference datasets are OISST-v2 for the thermal index (SST-based) and ERA5 for the dynamical (wind-based) indices. Note that the skill score values may be sensitive to the choice of the observational datasets to measure the model performance in some cases (Figure C1 in Appendix C). For instance, for most of sub-domains and indices, differences in skill scores computed with HadISST or OISST-v2 (ERA5 for dynamical indices) for UI^{sst} are as large as 250 points between the M skill scores computed with ERSST-v5 (NOAA-20CR-v3), but the slopes of the lines that connect the skill scores at different resolutions remain unchanged. Observational consistency is quantitatively assessed using the average of the M scores computed from each possible combination of pairs of observational datasets. This consistency is represented by the horizontal lines on panels in Fig.6. It is moderately high (above 300 points) for the thermal index (top panels) and Ekman transport (central panels) in most of the sub-regions analyzed. However this value is very low for the Ekman pumping (Fig.6; bottom panels) in the case of IP and nMoUS. This feature indicates, for these sub-domains, a weaker similarity among the validation datasets. These results illustrate the challenge that exists in providing an accurate characterization of the upwelling systems in observations and reanalysis.

For UI^{sst} (top panels), the slopes of the lines that connect the group 1 and group 2 in the MoUS and SMUS (panels b, c and d) sub-regions are negative, indicating a higher skill for higher resolution (group 2). However, an opposite behavior is observed over the IP (panel a), where low resolution models present larger levels of skill. We note no robust change for the M scores between group 1* and group 2*. These results support the conclusions drawn from Fig.2 in section 4.1. Let's try now to decompose the total Ekman process: for the Ekman transport (Fig.6; central panels), again the slopes of the lines that connect M values indicate a higher skill for group 2 in the MoUS and SMUS. For group 1* and group 2* models results's are still limited in reaching systematic conclusions on the effect of enhanced resolution in the atmospheric component although the MPI-ESM1-2-HR clearly shows larger skill score than its LR version in the nMoUS and SMUS sub-regions. Along the IP sub-region, the M scores are not conclusive, except for the CNRM-CM61-HR which provides a higher score with increased resolution.

Results regarding the Ekman pumping (Fig.6; bottom panels) are similar to those obtained for the Ekman transport, with improved model performance as the both resolutions increases and no systematic response when only the atmospheric grid resolution is modified. However, M values are broadly lower for the Ekman pumping than for the Ekman transport, indicating that models are less efficient in capturing the Ekman pumping than the transport along the coast. The conclusions obtained

from the M scores corroborate the results found in the previous section for the individual upwelling indices.

To summarize, increasing both the ocean and atmosphere resolution yields a higher skill score than the group 1 in the Morocco and SMUS upwelling systems, but no significant improvement in simulating the Iberian Peninsula upwelling system is found. On the other hand within the investigated range, increasing atmosphere resolution has a limited effect on the skill scores. Nevertheless, it is necessary to note that only two models form this group 2*, which make it difficult to extract a significant relationship between increased atmosphere resolution and model performance.

5   Summary and Conclusions

This study provides the first attempt to systematically evaluate the effect of increasing global model resolution (both in the atmosphere and ocean components) on the representation of the CUS. We have analyzed the historical simulations from six global climate models following the HighResMIP protocol (Haarsma et al., 2016). Four upwelling indices based on SSTs, wind stress and sea surface height have been used as metrics to assess the effects of increased models resolution. A quantitative skill metric, the Arcsin mean skill score, has also been applied to measure the models performance with respect to observational datasets. The most relevant findings can be summarised as follows:

Globally, our results show that observations and reanalysis yielding a fairly consistent picture of the CUS climatology. However in the southern part of Morocco and in the Senegalo-Mauritanian areas, upwelling indices derived from the validation datasets at lower resolution (ERSST-v5 and NOAA-20CR-v3) show greater magnitudes than those derived from the higher resolution datasets. The average of the M skill scores used to quantify the consistency among observational and reanalysis datasets at different resolutions is not very high. This highlights the challenge that exists for choosing a proper observational dataset to evaluate global climate models performance.

The impact of increasing model resolution is not the same in the different sub-domains of the CUS. In the northern part, within the IP domain, the high-resolution models do not seem to better simulate the structure of the climatological SSTs and the winds linked to the upwelling. For some models the LR version even produces better results than the HR version. However, in the southern CUS, and in particular in the MoUS and SMUS, the HR models show a clear improvement in the representation of upwelling indices. Increasing the resolution leads to simulations that are in better agreement with the observations. The best results are obtained when the resolution is increased for both components of the couple models, ocean and atmosphere. According to our results, the effect of increasing only the atmospheric resolution is not clear. This is probably mainly due to the fact that the sample analyzed in this case is small (only two models). The results presented here suggest nevertheless that increasing the resolution of the atmospheric component is not enough, and that it is also necessary to increase the resolution of the ocean to obtain a significant improvement in the representation of the CUS. The oceanic resolution emerges therefore as a key factor for having more realistic simulations, which is in agreement with other studies (e.g. Bryan et al., 2010; Putrasahan

et al., 2013; Parfitt et al., 2017 and Bellucci et al., 2021). Our results are also in line with previous modeling work suggesting that an increased resolution improve global climate model performance. Roberts et al. (2019) have shown that, increased model resolution in the atmosphere and ocean can have considerable impact on the large tropical Atlantic biases seen in typical CMIP-resolution models of the mean state and variability, both at the surface in terms of temperature, as well as in the deeper ocean.

490 According to Czaja et al. (2019), a clear dependence on resolution (both ocean and atmosphere) is found and better agreement with reanalysis and observations. However, this issue may also be model and region dependent (Delworth et al., 2012 and Raj et al., 2019). In the present study, the representation of oceanic processes related to upwelling has not been investigated in detail. Further work is needed to better understand the role of the ocean dynamic on the simulated upwelling improvements, in particular for comparing groups 1 and 2. The effect of stratification in particular is not investigated in this study. Comparing

495 ocean stratification and vertical transport between groups 1 and 2 can indeed provide insight into the relative role of increased ocean and atmospheric resolution in improving the representation of upwelling.

This study provides encouraging results for high-resolution global climate modelling, although many aspects related to the physical processes must be further assessed in the future. However, as already argued in previous studies that have analyzed

500 HighResMIP simulations (Bador et al., 2020; Moreno-Chamarro et al., 2022 and López-Parages and Terray, 2022), increasing the resolution of a global climate model does not necessarily have to be the only way to better represent the climate system. There is still much work to be done in terms of physical parameterizations as suggested by Patricola et al. (2012) and Harlaß et al. (2018). The improvements in model parametrizations and process representations, specific corrections applied to models, additional tuning, and longer spin-ups might all be essential. On the other hand, climate variability is particularly important

505 in the near term, and for highly variable quantities such as precipitation. But this might not be the case of coastal upwelling. Indeed, individual members of high resolution model show no difference to simulate the Canary upwelling system (not shown). We might infer that individual model runs do not necessarily represent independent estimates and therefore, it may be more convenient to only run a small subset of ensemble members for models at high resolution (although computationally expensive) than a large subset of ensemble members for models at standard resolution. This and other related question must be necessarily

510 faced in future works.

Code and data availability. All of the HighResMIP/PRIMAVERA model output analyzed in this manuscript is openly available from the Earth System Grid Federation (ESGF; https://esgf-index1.ceda.ac.uk/search/cmip6-ceda/) via the references. The SSTs products used in this analysis are available at https://psl.noaa.gov. The wind products are available via https://podaac.jpl.nasa.gov and https://apps.ecmwf.int/datasets/data/interim-full-daily. The SSH datasets used in this manuscript are currently available at https://www.esrl.noaa.gov/psd/gridd ed/data.godas.html and

515 https://www.aviso.altimetry.fr/en/data.html.

Author contributions. AS is the first author of the manuscript and performed the largest part of the analysis. ESG, JM and JLP are contributed with the ideas and writing and approved the submitted version.

Competing interests. The authors declare that there is no conflict of interests regarding the publication of this paper.

Acknowledgements. This work is carried out as part of TRIATLAS project (South and Tropical Atlantic climate-based marine ecosystem prediction for sustainable management) funded by the European Union's Horizon 2020 research and innovation programme under grant agreement No 817578.

520

References

Alvarez, I., deCastro, M., Gomez-Gesteira, M., and Prego, R.: Inter-and intra-annual analysis of the salinity and temperature evolution in the Galician Rias Baixas-ocean boundary (northwest Spain), J. Geophys. Res., 110, C04008, doi:10.1029/2004JC002504., 2005.

525   Alvarez, I., Gomez-Gesteira, M., deCastro, M., and Dias, J. M.: Spatiotemporal evolution of upwelling regime along the western coast of the Iberian Peninsula, Journal of Geophysical Research, 113, https://doi.org/10.1029/2008jc004744, 2008.

Arístegui, J., Barton, E. D., Tett, P., Montero, M. F., García-Muñoz, M., Basterretxea, G., Cussatlegras, A.-S., Ojeda, A., and de Armas, D.: Variability in plankton community structure, metabolism, and vertical carbon fluxes along an upwelling filament (Cape Juby, NW Africa), Progress in Oceanography, 62, 95 – 113, https://doi.org/https://doi.org/10.1016/j.pocean.2004.07.004, the Canary Islands Coastal

530   Transition Zone - Upwelling, Eddies and Filaments, 2004.

Arístegui, J., Barton, E. D., Álvarez-Salgado, X. A., Santos, A. M. P., Figueiras, F. G., Kifani, S., Hernández-León, S., Mason, E., Machú, E., and Demarcq, H.: Sub-regional ecosystem variability in the Canary Current upwelling, Progress in Oceanography, 83, 33–48, https://doi.org/10.1016/j.pocean.2009.07.031, 2009.

Atlas, R., Hoffman, R. N., Ardizzone, J., Leidner, S. M., Jusem, J. C., Smith, D. K., and Gombos, D.: A Cross-calibrated, Multiplatform

535   Ocean Surface Wind Velocity Product for Meteorological and Oceanographic Applications, Bulletin of the American Meteorological Society, 92, 157–174, https://doi.org/10.1175/2010bams2946.1, 2011.

Bador, M., Boe, J., Terray, L., Alexander, L., Baker, A., Koenigk, T., Putrasahan, D., Roberts, M., Scoccimarro, E., Schiemann, R., Seddon, J., Senan, R., and Valcke, S.: Impact of higher spatial atmospheric resolution on precipitation extremes over land in global climate models., J Geophys Res 125:e2019JD032184. https://doi.org/10.1029/2019JD032184, 2020.

540   Bakun, A.: Coastal upwelling indices, west coast of North America,, 1946-71. U.S. Dep. Commer., NOAA Tech. Rep. NMFS SSRF-671, 103 pp, 1973.

Bakun, A.: Coastal Ocean Upwelling, Science, 247, 198–201, https://doi.org/10.1126/science.247.4939.198, 1990.

Bakun, A. and Nelson, C. S.: The Seasonal Cycle of Wind-Stress Curl in Subtropical Eastern Boundary Current Regions, Journal of Physical Oceanography, 21, 1815–1834, https://doi.org/10.1175/1520-0485(1991)021<1815:tscows>2.0.co;2, 1991.

545   Balaguru, K., Van Roekel, L. P., Leung, L. R., and Veneziani, M.: Subtropical Eastern North Pacific SST bias in earth system models, Journal of Geophysical Research: Oceans, 126, e2021JC017 359, 2021.

Barton, E., Arı́stegui, J., Tett, P., Cantón, M., Garcı́a-Braun, J., Hernández-León, S., Nykjaer, L., Almeida, C., Almunia, J., Ballesteros, S., Basterretxea, G., Escánez, J., Garcı́a-Weill, L., Hernández-Guerra, A., López-Laatzen, F., Molina, R., Montero, M., Navarro-Pérez, E., Rodrı́guez, J., Van Lenning, K., Vélez, H., and Wild, K.: The transition zone of the Canary current upwelling region., Prog. Oceanogr.

550   41: 455–504., 1998.

Barton, E., Field, D., and Roy, C.: Canary current upwelling: More or less?, Progress in Oceanography, 116, 167–178, https://doi.org/10.1016/j.pocean.2013.07.007, 2013.

Bellucci, A., Athanasiadis, P. J., Scoccimarro, E., Ruggieri, P., Gualdi, S., Fedele, G., Haarsma, R. J., Garcia-Serrano, J., Castrillo, M., Putrahasan, D., Sanchez-Gomez, E., Moine, M.-P., Roberts, C. D., Roberts, M. J., Seddon, J., and Vidale, P. L.: Air-Sea interaction over the Gulf

555   Stream in an ensemble of HighResMIP present climate simulations, Climate Dynamics, 56, 2093–2111, https://doi.org/10.1007/s00382-020-05573-z, 2021.

Benazzouz, A., Mordane, S., Orbi, A., Chagdali, M., Hilmi, K., Atillah, A., Lluís Pelegrí, J., and Hervé, D.: An improved coastal upwelling index from sea surface temperature using satellite-based approach – The case of the Canary Current upwelling system, Continental Shelf Research, 81, 38–54, https://doi.org/10.1016/j.csr.2014.03.012, 2014.

560 Blanton, J. O., Atkinson, L. P., Castillejo, F., and Montero, A. L.: Coastal upwelling of the Rias Bajas, Galicia, northwest Spain,, I; hydrographic studies,Rapp.P.V.Reun.Cons.Int.Explor.Mer.,183,179–190., 1984.

Blanton, J. O., Tenore, K. R., Castillejo, F., Atkinson, L. P., Schwing, F. B., and Lavin, A.: The relationship of upwelling to mussel production in the rias on the western coast of Spain, Journal of Marine Research, 45, 497–511, https://doi.org/10.1357/002224087788401115, 1987.

Bravo, L., Ramos, M., Astudillo, O., Dewitte, B., and Goubanova, K.: Seasonal variability of the Ekman transport and pumping in the
565 upwelling system off central-northern Chile ($\sim 30°$S) based on a high-resolution atmospheric regional model (WRF), Ocean Science, 12, 1049–1065, https://doi.org/10.5194/os-12-1049-2016, 2016.

Bryan, F. O., Tomas, R., Dennis, J. M., Chelton, D. B., Loeb, N. G., and McClean, J. L.: Frontal Scale Air–Sea Interaction in High-Resolution Coupled Climate Models, Journal of Climate, 23, 6277–6291, https://doi.org/10.1175/2010jcli3665.1, 2010.

Capet, X. J., Marchesiello, P., and McWilliams, J. C.: Upwelling response to coastal wind profiles, Geophysical Research Letters, 31, n/a–n/a,
570 https://doi.org/10.1029/2004gl020123, 2004.

Cardone, V. J., Greenwood, J. G., and Cane, M. A.: On trends in historical marine wind data, J. Clim., 3(1), 113–127., 1990.

Castaño Tierno, A.: PhD Thesis: Tropical ocean-atmosphere interactions in coupled models. The case of of the Equatorial thermocline and the northwest African upwelling, 2020.

Cropper, T. E., Hanna, E., and Bigg, G. R.: Spatial and temporal seasonal trends in coastal upwelling off Northwest Africa, 1981–2012, Deep
575 Sea Research Part I: Oceanographic Research Papers, 86, 94–111, https://doi.org/10.1016/j.dsr.2014.01.007, 2014.

Czaja, A., Frankignoul, C., Minobe, S., and Vannière, B.: Simulating the midlatitude atmospheric circulation: what might we gain from high-resolution modeling of air-sea interactions?, Current Climate Change reports, 5, 390–406, 2019.

Davey, M., Huddleston, M., Sperber, K., Braconnot, P., Bryan, F., Chen, D., Colman, R., Cooper, C., Cubasch, U., Delecluse, P., DeWitt, D., Fairhead, L., Flato, G., Gordon, C., Hogan, T., Ji, M., Kimoto, M., Kitoh, A., Knutson, T., Latif, M., Treut, H. L., Li, T., Manabe, S.,
580 Mechoso, C., Power, S., Roeckner, E., Terray, L., Vintzileos, A., Voss, R., Wang, B., Washington, W., Yoshikawa, I., Yu, J., Yukimoto, S., Zebiak, S., and Meehl, G.: STOIC: a study of coupled model climatology and variability in tropical ocean regions, Climate Dynamics, 18, 403–420, https://doi.org/10.1007/s00382-001-0188-6, 2002.

de Boyer Montégut, C.: Mixed layer depth over the global ocean: An examination of profile data and a profile-based climatology, Journal of Geophysical Research, 109, https://doi.org/10.1029/2004jc002378, 2004.

585 deCastro, M., Gomez-Gesteira, M., Alvarez, I., Cabanas, J. M., and Prego, R.: Characterization of fall-winter upwelling recurrence along the Galician western coast (NW Spain) from 2000 to 2005: Dependence on atmospheric forcing,, J. Mar. Syst., 72, 145 – 158, doi:10.1016/j.jmarsys.2007.04.005., 2008a.

deCastro, M., Gómez-Gesteira, M., Lorenzo, M., Alvarez, I., and Crespo, A.: Influence of atmospheric modes on coastal upwelling along the western coast of the Iberian Peninsula, 1985 to 2005, Climate Research, 36, 169–179, https://doi.org/10.3354/cr00742, 2008b.

590 Delworth, T. L., Rosati, A., Anderson, W., Adcroft, A. J., Balaji, V., Benson, R., Dixon, K., Griffies, S. M., Lee, H.-C., Pacanowski, R. C., Vecchi, G. A., Wittenberg, A. T., Zeng, F., and Zhang, R.: Simulated Climate and Climate Change in the GFDL CM2.5 High-Resolution Coupled Climate Model, Journal of Climate, 25, 2755–2781, https://doi.org/10.1175/jcli-d-11-00316.1, 2012.

Doi, T., Vecchi, G. A., Rosati, A. J., and Delworth, T. L.: Biases in the Atlantic ITCZ in seasonal–interannual variations for a coarse-and a high-resolution coupled climate model, Journal of Climate, 25, 5494–5511, 2012.

595 Ducet, N., Le Traon, P. Y., and Reverdin, G.: Global high-resolution mapping of ocean circulation from TOPEX/Poseidon and ERS-1 and -2, Journal of Geophysical Research: Oceans, 105, 19 477–19 498, https://doi.org/10.1029/2000jc900063, 2000.

Exarchou, E., Prodhomme, C., Brodeau, L., Guemas, V., and Doblas-Reyes, F.: Origin of the warm eastern tropical Atlantic SST bias in a climate model, Climate Dynamics, 51, 1819–1840, 2018.

Faye, S., Lazar, A., Sow, B. A., and Gaye, A. T.: A model study of the seasonality of sea surface temperature and circulation in the Atlantic
600 North-eastern Tropical Upwelling System, Frontiers in Physics, 3, https://doi.org/10.3389/fphy.2015.00076, 2015.

Fraga, F.: Upwelling off the Galician Coast, Northwest Spain, in Coastal Upwelling, Coastal Estuarine, Stud., vol. 1, edited by F. A. Richards, pp. 176–182, AGU, Washington, D. C., 1981.

Freilich, M. H., D. G. L. and Spencer, M. W.: SeaWinds: A scanning scatterometer for ADEOS II—Science overview, Proc. Int. Geoscience and Remote Sensing Symp., Pasadena, CA, IEEE, 960–963., 1994.

605 Gent, P. R., Yeager, S. G., Neale, R. B., Levis, S., and Bailey, D. A.: Improvements in a half degree atmosphere/land version of the CCSM, Climate Dynamics, 34, 819–833, 2010.

Gomez-Gesteira, M., Moreira, C., Alvarez, I., and deCastro, M.: Ekman transport along the Galician coast (northwest Spain) calculated from forecasted winds, Journal of Geophysical Research, 111, https://doi.org/10.1029/2005jc003331, 2006.

Gómez-Gesteira, M., de Castro, M., Álvarez, I., Lorenzo, M. N., Gesteira, J. L. G., and Crespo, A. J. C.: Spatio-temporal Up-
610 welling Trends along the Canary Upwelling System (1967-2006), Annals of the New York Academy of Sciences, 1146, 320–337, https://doi.org/10.1196/annals.1446.004, 2008.

Gutjahr, O., Putrasahan, D., Lohmann, K., Jungclaus, J. H., von Storch, J.-S., Brüggemann, N., Haak, H., and Stössel, A.: Max Planck Institute Earth System Model (MPI-ESM1.2) for the High-Resolution Model Intercomparison Project (HighResMIP), Geoscientific Model Development, 12, 3241–3281, https://doi.org/10.5194/gmd-12-3241-2019, 2019.

615 Haarsma, R., Acosta, M., Bakhshi, R., Bretonnière, P.-A. B., Caron, L.-P., Castrillo, M., Corti, S., Davini, P., Exarchou, E., Fabiano, F., Fladrich, U., Franco, R. F., García-Serrano, J., von Hardenberg, J., Koenigk, T., Levine, X., Meccia, V., van Noije, T., van den Oord, G., Palmeiro, F. M., Rodrigo, M., Ruprich-Robert, Y., Sager, P. L., Tourigny, É., Wang, S., van Weele, M., and Wyser, K.: HighResMIP versions of EC-Earth: EC-Earth3P and EC-Earth3P-HR. Description, model performance, data handling and validation, https://doi.org/10.5194/gmd-2019-350, 2020.

620 Haarsma, R. J., Roberts, M. J., Vidale, P. L., Senior, C. A., Bellucci, A., Bao, Q., Chang, P., Corti, S., Fučkar, N. S., Guemas, V., von Harden-berg, J., Hazeleger, W., Kodama, C., Koenigk, T., Leung, L. R., Lu, J., Luo, J.-J., Mao, J., Mizielinski, M. S., Mizuta, R., Nobre, P., Satoh, M., Scoccimarro, E., Semmler, T., Small, J., and von Storch, J.-S.: High Resolution Model Intercomparison Project (HighResMIP v1.0) for CMIP6, Geoscientific Model Development, 9, 4185–4208, https://doi.org/10.5194/gmd-9-4185-2016, 2016.

Harlass, J., Latif, M., and Park, W.: Improving climate model simulation of tropical Atlantic sea surface temperature: The importance of
625 enhanced vertical atmosphere model resolution, Geophysical Research Letters, 42, 2401–2408, 2015.

Harlaß, J., Latif, M., and Park, W.: Alleviating tropical Atlantic sector biases in the Kiel climate model by enhancing horizontal and vertical atmosphere model resolution: climatology and interannual variability, Climate Dynamics, 50, 2605–2635, https://doi.org/10.1007/s00382-017-3760-4, 2018.

Herbland, A. et al.: La production primaire dans l'upwelling mauritanien en mars 1973, 1974.

630 Hersbach, H., Bell, B., Berrisford, P., Hirahara, S., Horányi, A., Muñoz-Sabater, J., Nicolas, J., Peubey, C., Radu, R., Schepers, D., Simmons, A., Soci, C., Abdalla, S., Abellan, X., Balsamo, G., Bechtold, P., Biavati, G., Bidlot, J., Bonavita, M., Chiara, G., Dahlgren, P., Dee, D., Dia-mantakis, M., Dragani, R., Flemming, J., Forbes, R., Fuentes, M., Geer, A., Haimberger, L., Healy, S., Hogan, R. J., Hólm, E., Janisková,

M., Keeley, S., Laloyaux, P., Lopez, P., Lupu, C., Radnoti, G., Rosnay, P., Rozum, I., Vamborg, F., Villaume, S., and Thépaut, J. N.: The ERA5 global reanalysis, Quarterly Journal of the Royal Meteorological Society, 146, 1999– 2049. https://doi.org/10.1002/qj.3803, 2020.

635   Hewitt, H. T., Roberts, M., Mathiot, P., Biastoch, A., Blockley, E., Chassignet, E. P., Fox-Kemper, B., Hyder, P., Marshall, D. P., Popova, E., Treguier, A.-M., Zanna, L., Yool, A., Yu, Y., Beadling, R., Bell, M., Kuhlbrodt, T., Arsouze, T., Bellucci, A., Castruccio, F., Gan, B., Putrasahan, D., Roberts, C. D., Roekel, L. V., and Zhang, Q.: Resolving and Parameterising the Ocean Mesoscale in Earth System Models, Current Climate Change Reports, 6, 137–152, https://doi.org/10.1007/s40641-020-00164-w, 2020.

Huang, B., Thorne, P. W., Banzon, V. F., Boyer, T. P., Chepurin, G. A., Lawrimore, J. H., Menne, M. J., Smith, T. M., Vose, R. S., and Zhang,
640   H.-M.: Extended Reconstructed Sea Surface Temperature, Version 5 (ERSSTv5): Upgrades, Validations, and Intercomparisons, 2017.

Huyer, A.: Coastal upwelling in the California current system, Progress in Oceanography, 12, 259 – 284, https://doi.org/https://doi.org/10.1016/0079-6611(83)90010-1, 1983.

Jacox, M., Moore, A., Edwards, C., and Fiechter, J.: Spatially resolved upwelling in the California Current System and its connections to climate variability, Geophysical Research Letters, 41, 3189–3196, 2014.

645   Jacox, M. G., Edwards, C. A., Hazen, E. L., and Bograd, S. J.: Coastal Upwelling Revisited: Ekman, Bakun, and Improved Upwelling Indices for the U.S. West Coast, Journal of Geophysical Research: Oceans, 123, 7332–7350, https://doi.org/10.1029/2018jc014187, 2018.

Lathuilière, C., Echevin, V., and Lévy, M.: Seasonal and intraseasonal surface chlorophyll-a variability along the northwest African coast, Journal of Geophysical Research, 113, https://doi.org/10.1029/2007jc004433, 2008.

López-Parages, J. and Terray, L.: Tropical North Atlantic Response to ENSO: Sensitivity to Model Spatial Resolution, Journal of Climate,
650   35, 3–16, 2022.

Ma, J., Xu, S., and Wang, B.: Warm bias of sea surface temperature in Eastern boundary current regions—a study of effects of horizontal resolution in CESM, Ocean Dynamics, 69, 939–954, https://doi.org/10.1007/s10236-019-01280-4, 2019.

Manabe, S., Stouffer, R. J., Spelman, M. J., and Bryan, K.: Transient Responses of a Coupled Ocean–Atmosphere Model to Gradual Changes of Atmospheric CO2. Part I. Annual Mean Response, Journal of Climate, 4, 785–818, https://doi.org/10.1175/1520-
655   0442(1991)004<0785:troaco>2.0.co;2, 1991.

Marcello, J., Hernández-Guerra, A., Eugenio, F., and Fonte, A.: Seasonal and temporal study of the northwest African upwelling system, International Journal of Remote Sensing, 32, 1843–1859, https://doi.org/10.1080/01431161003631576, 2011.

Marchesiello, P. and Estrade, P.: Upwelling limitation by onshore geostrophic flow, Journal of Marine Research, 68, 37–62, https://doi.org/10.1357/002224010793079004, 2010.

660   McGregor, H. V., Dima, M., Fischer, H. W., and Mulitza, S.: Rapid 20th-Century Increase in Coastal Upwelling off Northwest Africa, Science, 315, 637–639, https://doi.org/10.1126/science.1134839, 2007.

Minas, H., HJ, M., LA, C., and RC, D.: Nutrients and primary production in the upwelling region off Northwest Africa, 1982.

Mittelstaedt, E.: The ocean boundary along the northwest African coast: Circulation and oceanographic properties at the sea surface, Progress in Oceanography, 26, 307–355, https://doi.org/10.1016/0079-6611(91)90011-a, 1991.

665   Moreno-Chamarro, E., Caron, L.-P., Tomas, S. L., Vegas-Regidor, J., Gutjahr, O., Moine, M.-P., Putrasahan, D., Roberts, C. D., Roberts, M. J., Senan, R., Terray, L., Tourigny, E., and Vidale, P. L.: Impact of increased resolution on long-standing biases in HighResMIP-PRIMAVERA climate models, Geoscientific Model Development, 15, 269–289, https://doi.org/10.5194/gmd-15-269-2022, 2022.

Ndoye, S., Capet, X., Estrade, P., Sow, B., Machu, E., Brochier, T., Döring, J., and Brehmer, P.: Dynamics of a "low-enrichment high-retention" upwelling center over the southern Senegal shelf, Geophysical Research Letters, 44, 5034–5043,
670   https://doi.org/10.1002/2017gl072789, 2017.

Nykjær, L. and Van Camp, L.: Seasonal and interannual variability of coastal upwelling along northwest Africa and Portugal from 1981 to 1991, Journal of Geophysical Research, 99, 14 197, https://doi.org/10.1029/94jc00814, 1994.

Oerder, V., Colas, F., Echevin, V., Codron, F., Tam, J., and Belmadani, A.: Peru-Chile upwelling dynamics under climate change, Journal of Geophysical Research: Oceans, 120, 1152–1172, https://doi.org/10.1002/2014jc010299, 2015.

675 Parfitt, R., Czaja, A., and Kwon, Y.-O.: The impact of SST resolution change in the ERA-Interim reanalysis on wintertime Gulf Stream frontal air-sea interaction, Geophysical Research Letters, 44, 3246–3254, 2017.

Patricola, C. M., Li, M., Xu, Z., Chang, P., Saravanan, R., and Hsieh, J.-S.: An investigation of tropical Atlantic bias in a high-resolution coupled regional climate model, Climate Dynamics, 39, 2443–2463, https://doi.org/10.1007/s00382-012-1320-5, 2012.

Pauly, D. and Christensen, V.: Primary production required to sustain global fisheries, Nature, 374, 255–257, 680 https://doi.org/10.1038/374255a0, 1995.

Pennington, J., Mahoney, K., Kuwahara, V., Kolber, D., Calienes, R., and Chavez, F.: Primary production in the easterntropical Pacific, Progress in Oceanography 69 (2–4), 285–317, 2006.

Pickett, M. H.: Ekman transport and pumping in the California Current based on the U.S. Navy's high-resolution atmospheric model (COAMPS), Journal of Geophysical Research, 108, https://doi.org/10.1029/2003jc001902, 2003.

685 Pires, A. C., Nolasco, R., Rocha, A., and Dubert, J.: Assessing future climate change in the Iberian Upwelling System, Journal of Coastal Research, 165, 1909–1914, https://doi.org/10.2112/si65-323.1, 2013.

Putrasahan, D., Lohmann, K., von Storch, J.-S., Jungclaus, J. H., Gutjahr, O., and Haak, H.: Surface flux drivers for the slowdown of the Atlantic meridional overturning circulation in a high-resolution global coupled climate model, Journal of Advances in Modeling Earth Systems, 11, 1349–1363, 2019.

690 Putrasahan, D. A., Miller, A. J., and Seo, H.: Isolating mesoscale coupled ocean–atmosphere interactions in the Kuroshio Extension region, Dynamics of Atmospheres and Oceans, 63, 60–78, https://doi.org/https://doi.org/10.1016/j.dynatmoce.2013.04.001, 2013.

Raj, J., Bangalath, H. K., and Stenchikov, G.: West African Monsoon: current state and future projections in a high-resolution AGCM, Climate Dynamics, 52, 6441–6461, https://doi.org/10.1007/s00382-018-4522-7, 2019.

Renault, L., Deutsch, C., McWilliams, J. C., Frenzel, H., Liang, J.-H., and Colas, F.: Partial decoupling of primary productivity from up- 695 welling in the California Current system, Nature Geoscience, 9, 505–508, https://doi.org/10.1038/ngeo2722, 2016.

Reynolds, R. W., Smith, T. M., Liu, C., Chelton, D. B., Casey, K. S., and Schlax, M. G.: Daily High-Resolution-Blended Analyses for Sea Surface Temperature, Journal of Climate, 20, 5473–5496, https://doi.org/10.1175/2007jcli1824.1, 2007.

Richter, I.: Climate model biases in the eastern tropical oceans: causes, impacts and ways forward, Wiley Interdisciplinary Reviews: Climate Change, 6, 345–358, https://doi.org/10.1002/wcc.338, 2015.

700 Richter, I. and Xie, S.-P.: On the origin of equatorial Atlantic biases in coupled general circulation models, Climate Dynamics, 31, 587–598, https://doi.org/10.1007/s00382-008-0364-z, 2008.

Richter, I., Xie, S.-P., Wittenberg, A. T., and Masumoto, Y.: Tropical Atlantic biases and their relation to surface wind stress and terrestrial precipitation, Climate Dynamics, 38, 985–1001, https://doi.org/10.1007/s00382-011-1038-9, 2012.

Roberts, C. D., Senan, R., Molteni, F., Boussetta, S., Mayer, M., and Keeley, S. P. E.: Climate model configurations of the ECMWF 705 Integrated Forecasting System (ECMWF-IFS cycle 43r1) for HighResMIP, Geoscientific Model Development, 11, 3681–3712, https://doi.org/10.5194/gmd-11-3681-2018, 2018.

Roberts, M. J., Hewitt, H. T., Hyder, P., Ferreira, D., Josey, S. A., Mizielinski, M., and Shelly, A.: Impact of ocean resolution on coupled air-sea fluxes and large-scale climate, Geophys. Res. Lett., 43, 10,430–10,438,doi:10.1002/ 2016GL070559, 2016.

Roberts, M. J., Baker, A., Blockley, E. W., Calvert, D., Coward, A., Hewitt, H. T., Jackson, L. C., Kuhlbrodt, T., Mathiot, P., Roberts, C. D., Schiemann, R., Seddon, J., Vannière, B., and Vidale, P. L.: Description of the resolution hierarchy of the global coupled HadGEM3-GC3.1 model as used in CMIP6 HighResMIP experiments, Geoscientific Model Development, 12, 4999–5028, https://doi.org/10.5194/gmd-12-4999-2019, 2019.

Rossi, V., Feng, M., Pattiaratchi, C., Roughan, M., and Waite, A. M.: On the factors influencing the development of sporadic upwelling in the Leeuwin Current system, Journal of Geophysical Research: Oceans 118, 3608–3621. https://doi.org/10.1002/jgrc.20242, 2013.

Rykaczewski, R. R., Dunne, J. P., Sydeman, W. J., García-Reyes, M., Black, B. A., and Bograd, S. J.: Poleward displacement of coastal upwelling-favorable winds in the ocean's eastern boundary currents through the 21st century, Geophysical Research Letters, 42, 6424–6431, https://doi.org/10.1002/2015gl064694, 2015.

Santos, A. M. P., Kazmin, A. S., and Peliz, Á.: Decadal changes in the Canary upwelling system as revealed by satellite observations: Their impact on productivity, Journal of Marine Research, 63, 359–379, https://doi.org/10.1357/0022240053693671, 2005.

Santos, F., deCastro, M., Gómez-Gesteira, M., and Álvarez, I.: Differences in coastal and oceanic SST warming rates along the Canary upwelling ecosystem from 1982 to 2010, Continental Shelf Research, 47, 1–6, https://doi.org/10.1016/j.csr.2012.07.023, 2012.

Schwing, F. B., O'Farrell, M., Steger, J. M., and Baltz, K.: Coastal upwelling indices, west coast of North America, 1946-1995, Tech. Memo. NOAA-TM-NMFS-SWFSC-231, 144 pp., NOAA, La Jolla, Calif., 1996.

Slivinski, L. C., Compo, G. P., Whitaker, J. S., Sardeshmukh, P. D., Giese, B. S., McColl, C., Allan, R., Yin, X., Vose, R., Titchner, H., Kennedy, J., Spencer, L. J., Ashcroft, L., Brönnimann, S., Brunet, M., Camuffo, D., Cornes, R., Cram, T. A., Crouthamel, R., Domínguez-Castro, F., Freeman, J. E., Gergis, J., Hawkins, E., Jones, P. D., Jourdain, S., Kaplan, A., Kubota, H., Blancq, F. L., Lee, T.-C., Lorrey, A., Luterbacher, J., Maugeri, M., Mock, C. J., Moore, G. K., Przybylak, R., Pudmenzky, C., Reason, C., Slonosky, V. C., Smith, C. A., Tinz, B., Trewin, B., Valente, M. A., Wang, X. L., Wilkinson, C., Wood, K., and Wyszyński, P.: Towards a more reliable historical reanalysis: Improvements for version 3 of the Twentieth Century Reanalysis system, Quarterly Journal of the Royal Meteorological Society, 145, 2876–2908, https://doi.org/10.1002/qj.3598, 2019.

Small, R. J., Bacmeister, J., Bailey, D., Baker, A., Bishop, S., Bryan, F., Caron, J., Dennis, J., Gent, P., Hsu, H.-m., et al.: A new synoptic scale resolving global climate simulation using the Community Earth System Model, Journal of Advances in Modeling Earth Systems, 6, 1065–1094, 2014.

Small, R. J., Curchitser, E., Hedstrom, K., Kauffman, B., and Large, W. G.: The Benguela Upwelling System: Quantifying the Sensitivity to Resolution and Coastal Wind Representation in a Global Climate Model*, Journal of Climate, 28, 9409–9432, https://doi.org/10.1175/jcli-d-15-0192.1, 2015.

Smith, R. L.: Upwelling, Oceanogr. Mar. Biol. Ann. Rev., 6, 11– 46, 1968.

Sverdrup, H. U., Johnson, M. W., and Fleming, R. H.: The Oceans, Their Physics, Chemistry and General Biology, 1060 pp., Prentice-Hall, Englewood Cliffs New Jersey, 1942.

Sylla, A., Mignot, J., Capet, X., and Gaye, A.: Weakening of the Senegalo–Mauritanian upwelling system under climate change, Climate Dynamics, 53, 4447–4473, https://doi.org/10.1007/s00382-019-04797-y, 2019.

Titchner, H. A. and Rayner, N. A.: The Met Office Hadley Centre sea ice and sea-surface temperature data set, version 2: 1. Sea ice concentrations., J. Geophys. Res., 119, 2864–2889, doi:10.1002/2013JD020316., 2014.

Torres, R.: Spatial patterns of wind and sea surface temperature in the Galician upwelling region, Journal of Geophysical Research, 108, https://doi.org/10.1029/2002jc001361, 2003.

Tretkoff, E.: Research Spotlight: Coastal cooling and marine productivity increasing off Peru, Eos, Transactions American Geophysical Union, 92, 184–184, 2011.

Van Camp, L., Nykjaer, L., Mittelstaedt, E., and Schlittenhardt, P.: Upwelling and boundary circulation off Northwest Africa as depicted by infrared and visible satellite observations, Progress in Oceanography, 26, 357–402, 1991.

750   Vanniere, B., Demory, M. E., Vidale, P. L., Schiemann, R., Roberts, M. J., Roberts, C. D., ., and Senan, R.: Multi-model evaluation of the sensitivity of the global energy budget and hydrological cycle to resolution., Climate Dynamics, 52(11), 6817-6846. https://doi.org/10.1007/s00382-018-4547-y, 2019.

Vazquez, R., Parras-Berrocal, I., Cabos, W., Sein, D. V., Mañanes, R., Perez, J. I., and Izquierdo, A.: Climate Evaluation of a High-Resolution Regional Model over the Canary Current Upwelling System, in: Lecture Notes in Computer Science, pp. 240–252, Springer International

755   Publishing, https://doi.org/10.1007/978-3-030-22747-0_19, 2019.

Voldoire, A., Saint-Martin, D., Sénési, S., Decharme, B., Alias, A., Chevallier, M., C. J., Guérémy, J. F., Michou, M., Moine, M. P., Nabat, P., Roehrig, R., Salas y Mélia, D., Séférian, R., Valcke, S., Beau, I., Belamari, S., Berthet, S., Cassou, C., Cattiaux, J., Deshayes, J., Douville, H., Ethé, C.and Franchistéguy, L., Geoffroy, O., Lévy, C., Madec, G., Meurdesoif, Y., Msadek, R., Ribes, A., Sanchez-Gomez, E., Terray, L., and Waldman, R.: Evaluation of CMIP6 DECK experiments with CNRM-CM6-1., Journal of Advances in Modeling Earth Systems,

760   11, 2177– 2213. https://doi.org/10.1029/2019MS001683, 2019.

Wang, D., Gouhier, T. C., Menge, B. A., and Ganguly, A. R.: Intensification and spatial homogenization of coastal upwelling under climate change, Nature, 518, 390–394, https://doi.org/10.1038/nature14235, 2015.

Williams, K. D., Copsey, D., Blockley, E. W., Bodas-Salcedo, A., Calvert, D., Comer, R., Davis, P., Graham, T., Hewitt, H. T., Hill, R., Hyder, P., Ineson, S., Johns, T. C., Keen, A. B., Lee, R. W., Megann, A., Milton, S. F., Rae, J. G. L., Roberts, M. J., Scaife, A. A., Schiemann,

765   R., Storkey, D., Thorpe, L., Watterson, I. G., Walters, D. N., West, A., Wood, R. A., Woollings, T., and Xavier, P. K.: The Met Office Global Coupled Model 3.0 and 3.1 (GC3.0 and GC3.1) Configurations, Journal of Advances in Modeling Earth Systems, 10, 357–380, https://doi.org/10.1002/2017ms001115, 2018.

Wooster, W., Bakun, A., and McLain, D. R.: SEASONAL UPWELLING CYCLE ALONG THE EASTERN BOUNDARY OF THE NORTH ATLANTIC., Journal of Marine Research, 34, 131–141, 1976.

770   Worley, S. J., Woodruff, S. D., Reynolds, R. W., Lubker, S. J., and Lott, N.: ICOADS release 2.1 data and products, International Journal of Climatology, 25, 823–842, https://doi.org/10.1002/joc.1166, 2005.

Yoshida, K.: Coastal Upwellig off the California coast, Rec. Oceanogr. Works Japan, 2,8-20, 1995.

Zuidema, P., Chang, P., Medeiros, B., Kirtman, B. P., Mechoso, R., Schneider, E. K., Toniazzo, T., Richter, I., Small, R. J., Bellomo, K., et al.: Challenges and prospects for reducing coupled climate model SST biases in the eastern tropical Atlantic and Pacific Oceans: The

775   US CLIVAR Eastern Tropical Oceans Synthesis Working Group, Bulletin of the American Meteorological Society, 97, 2305–2328, 2016.
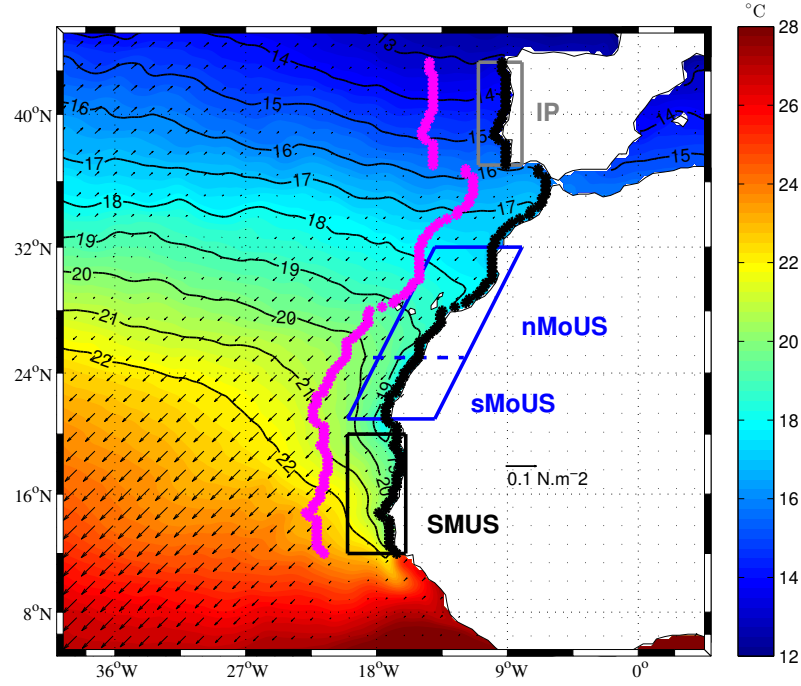
Figure 1. Colors: OISSTv2 climatological mean ($^\circ C$) in March averaged over 1992-2011 period. Black vectors show the wind stress from CCMP (computed offline from winds as described in Appendix). The referent vector is shown in land and the contours show some SST values. The grey box ($37^\circ N$-$43^\circ N$ and $8^\circ W$-$11^\circ W$) represents the Iberian Peninsula region (IP); the black box ($12^\circ N$-$20^\circ N$ and $16^\circ W$-$20^\circ W$) represents the Senegalo-Mauritanian subregion (SMUS). The inclined blue box outlines the the Morocco (MoUS) subdomain ($21^\circ N$-$32^\circ N$) with a blue dashed line representing the northern boundary of south Morocco subdomain (sMoUS). The stars indicate the coastal (black) and offshore (magenta) locations used for the computation of thermal upwelling index (see section 2. 3). The black and magenta dots are separated by 5° of longitude.
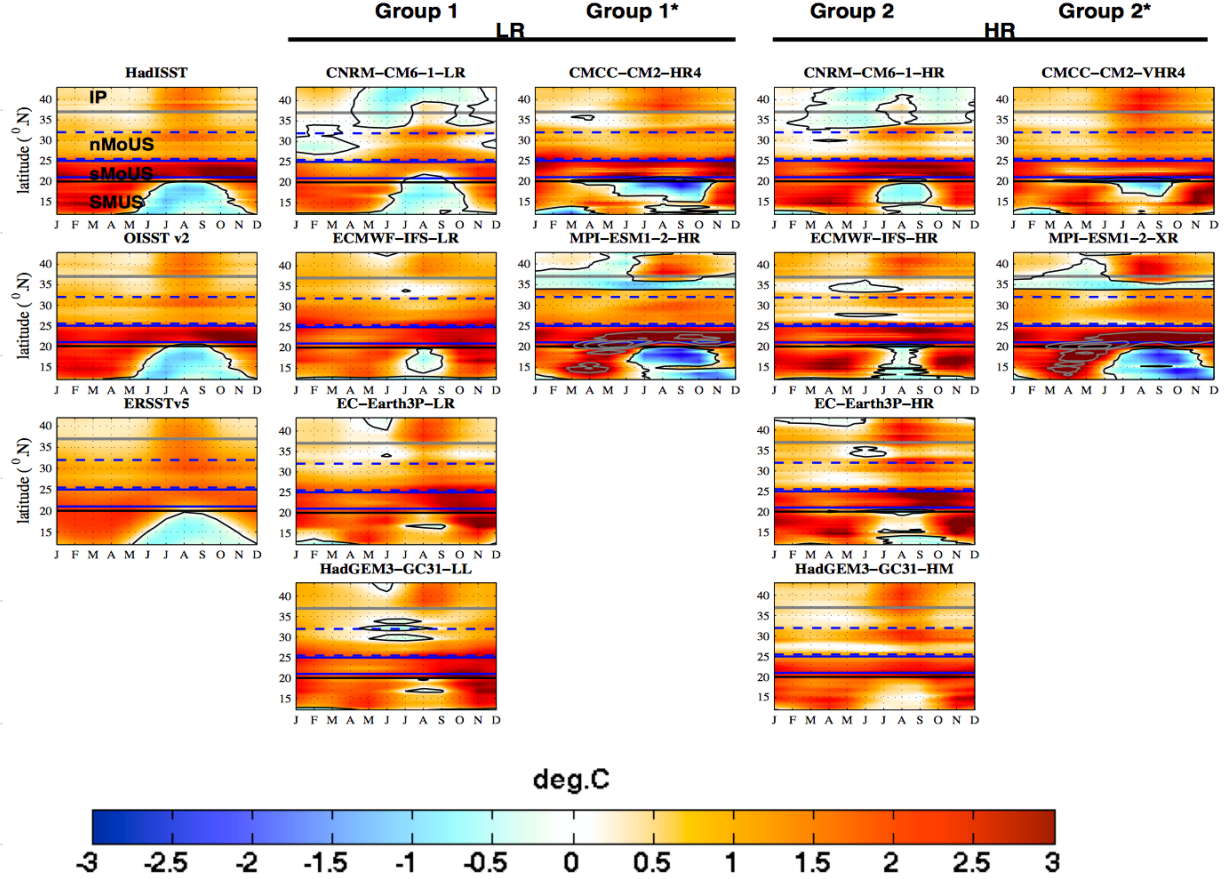
Figure 2. Latitude-time plot of UI^{sst} upwelling index ($^{\circ}C$) computed as explained in section 2.3. The time axis shows climatological months over the period 1985-2014 for several model configurations and reference datasets (HadISST, OISST v2 and ERSST v5). Following columns: models from the groups 1, 1*, 2 and 2* respectively (see section 2.1 for the definition of these groups). Positive (negative) values correspond to upwelling (downwelling) conditions. On each panel, the grey line represents the southern boundary of IP sub-region ($37^{\circ}N$-$43^{\circ}N$). The horizontal blue lines (dashed lines) are positioned at $21^{\circ}N$ and $25^{\circ}N$ ($26^{\circ}N$ and $32^{\circ}N$) and give the limitation of the sMoUS (nMoUS) and the black line represents the northern boundary of SMUS sub-region ($12^{\circ}N$-$20^{\circ}N$). The black (grey) contour shows the contour zero (values $> 3^{\circ}C$). This index is calculated over the models native grid.
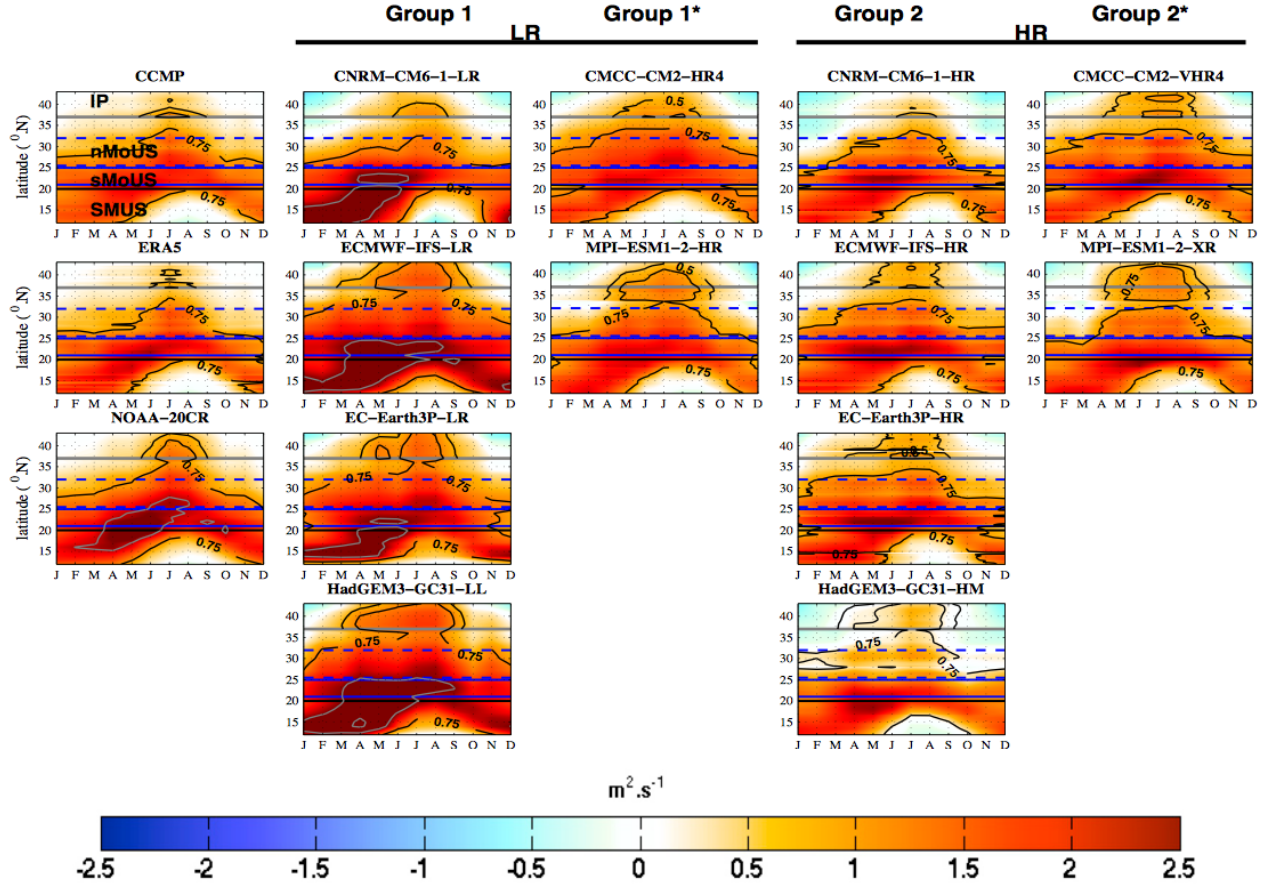
Figure 3. Latitude-time plot of $CSET$ upwelling index ($m^2 s^{-1}$) computed over the grid point located along the coast (black stars in Fig. 1). The time axis shows climatological months over the period 1985-2014 (1992-2011) for several model configurations and reference datasets: ERA5, NOAA-20CR-v3 (CCMP). Following columns: models from the groups 1, 1*, 2 and 2* respectively (see section 2.1 for the definition of these groups). Positive (negative) values correspond to upwelling (downwelling) conditions. On each panel, the grey line represents the southern boundary of IP sub-region (37°N-43°N). The horizontal blue lines (dashed lines) are positioned at 21°N and 25°N (26°N and 32°N) and give the limitation of the sMoUS (nMoUS) and the black line represents the northern boundary of SMUS subregion (12°N-20°N). The black (grey) contours show the contours $0.5 m^2 s^{-1}$ and $0.75 m^2 s^{-1}$ (values $> 2.5 m^2 s^{-1}$). This index is calculated over the models native grid
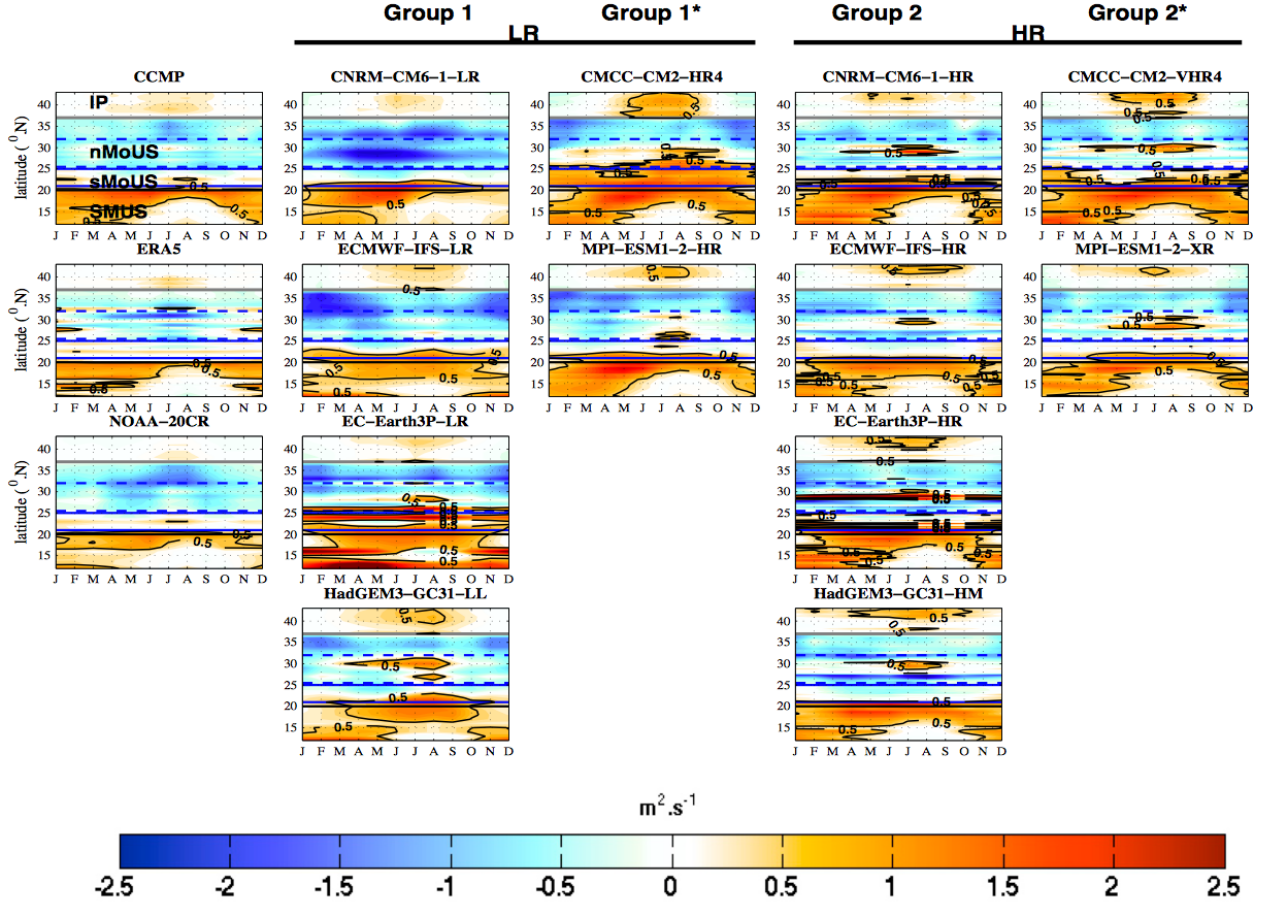
Figure 4. Latitude-time plot of integrated Ekman pumping ($m^2 s^{-1}$) calculated as explained in section 2. 3. The time axis shows climatological months over the period 1985-2014 (1992-2011) for several model configurations and reference datasets: ERA5, NOAA-20CR-v3 (CCMP). Following columns: models from the groups 1, 1*, 2 and 2* respectively (see section 2.1 for the definition of these groups). Positive (negative) values correspond to upwelling (downwelling) conditions. See Fig. 3 for comments on the horizontal lines and contours. This index is calculated over the models native grid
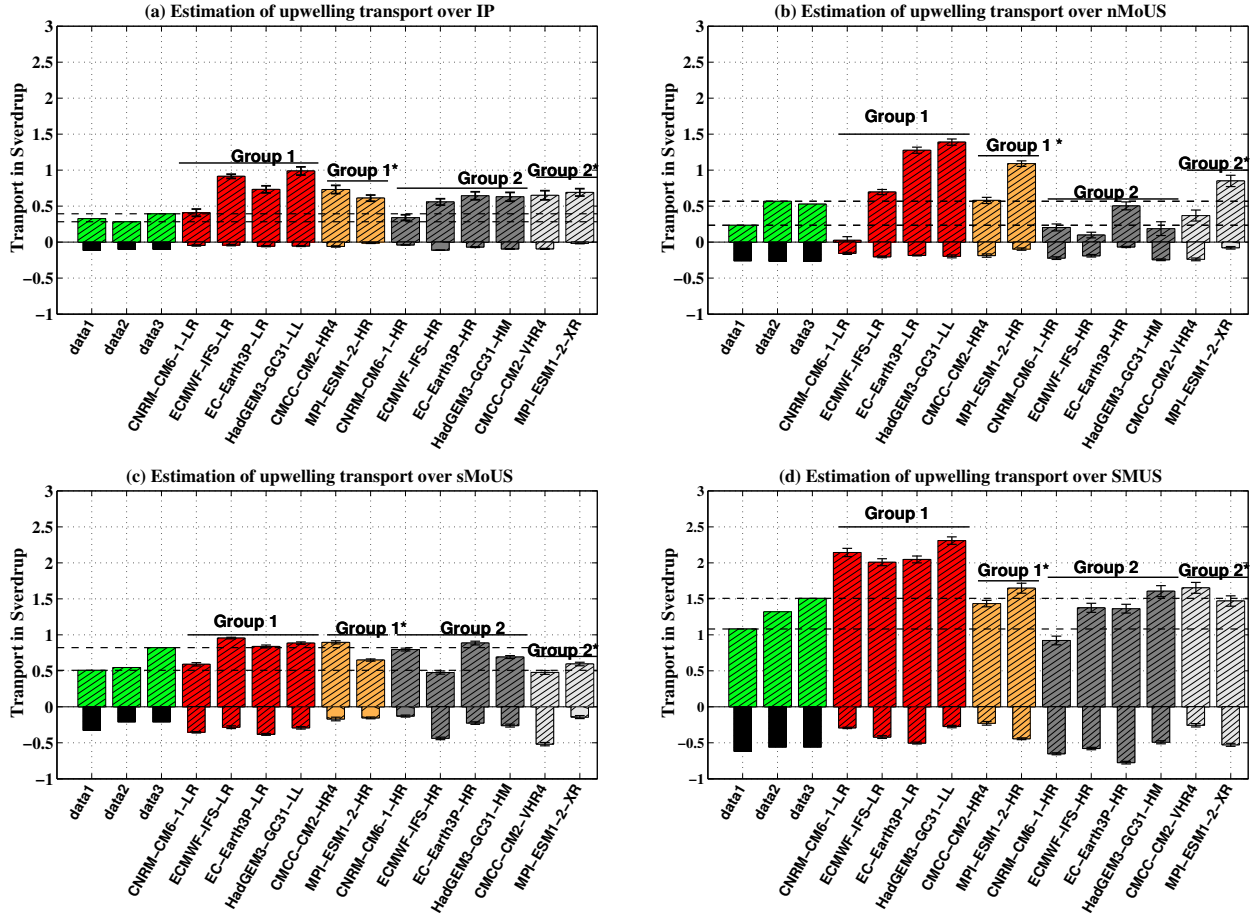
Figure 5. Negative bars: estimate of onshore geostrophic flow T_{geo} contribution (in Sverdrup, ±error bars: black whiskers bars) computed from Eq (7) and averaged from July to September over IP (panel a) and in nMoUS (panel b), all the year in sMoUS (panel c) and from November to May in the SMUS (panel d). The first black bar shows T_{geo} computed from AVISO satellite data period (1993-2005) and Mld de Boyer Montégut (2004), and the second and third black bars correspond to T_{geo} derived from the GODAS reanalysis (1985-2014) and the previous MLD data. The following columns show the results for the individual climate models. Positive bars show the total volume of upwelling water (UI_{total}) computed as the sum of the integrated contribution of the three dynamical indices ($CSET + W_{ek} + T_{geo}$) to the upwelling. Data 1 (1993-2005) corresponds to Ekman process computed from CCMP and T_{geo} from AVISO SSH product and MLD de Boyer Montegut. Data 2 and data 3 represent the Ekman process from ERA5 and NOAA-20CR-v3 over 1985-2014 respectively and T_{geo} from GODAS and the same MLD used in data 1. The horizontal discontinuous lines highlighted the observational range.
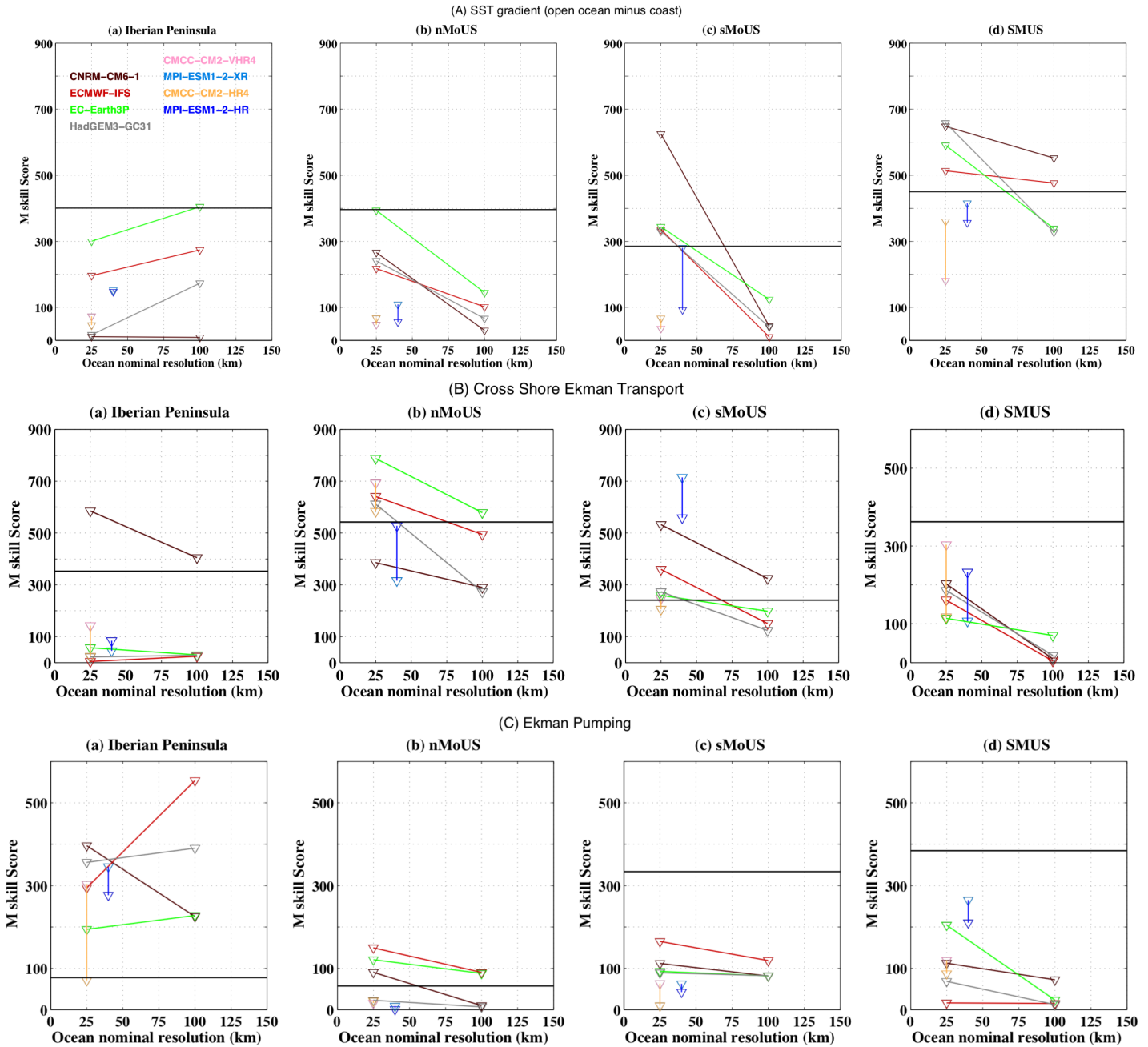
Figure 6. M skill score of SST gradient between ocean minus coast (top panels), Ekman transport (central panels) and Ekman pumping (bottom panels) as a function of the ocean model nominal resolution. The models from the group 1* and 2 * are thus represented by the vertical lines (with their HR version: MPI-ESM1-2-XR and CMCC-CM2-VHR4 highlighted by the light blue and magenta color respectively). The score is computed and averaged along the IP sub-region (panel a) and nMoUS (panel b) from July to September, all the year in sMoUS (panel c) and from November to May along the SMUS (panel d) over the period 1985-2014. For the SST index (dynamical indices), each model is evaluated to OISST-v2 (ERA5) observation. Horizontal line on the each panel correspond to the average of the M scores computed from all combinations of pair of observational products.

	Model name	Atmosphere nominal resolution	Ocean nominal resolution
Group 1 (LR-ocea/atm)	CNRM-CM6-1-LR	2.5°	1°
	ECMWF-IFS-LR	0.5°	1°
	EC-Earth3P-LR	1°	1°
	HadGEM3- GC31-LL	2.5°	1°
Group 1* (LR-atm)	CMCC-CM2-HR4	1°	0.25°.
	MPI-ESM-1-2-HR	1°	0.4°.
Group 2 (HR-ocea/atm)	CNRM-CM6-1-HR	0.5°	0.25°
	ECMWF-IFS-HR	0.25°	0.25°
	EC-Earth3P-HR	0.5°	0.25°
	HadGEM3- GC31-HM	0.5°	0.25°
Group 2* (HR-atm)	CMCC-CM2-VHR4	0.25°	0.25°
	MPI-ESM-1-2-XR	0.5°	0.4°.
Variables used: tos, tauuo, tauvo, zos, mlotst			

Table 1. List of the HighResMIP/PRIMAVERA models used in this study. The first and second columns list the groups and models used. The third and fourth columns indicate the atmosphere and ocean nominal resolution. The last row at the bottom of the table lists the variables that were used for our study: sea surface temperature (sst, called tos in HighResMIP database), zonal and meridional wind stress components (tauuo and tauvo), sea surface height (ssh, called zos), mixed layer depth (mld, called mlotst).

Variables used	Name of datasets	Period	spatial reoslution
SST (observations)	HadISST.2 (Titchner et al.2014)	1981-2016	0.25° x 0.25°
	OISSTv2 (Reynolds et 2007)	1982-2015	0.25° x 0.25°
	ERSST v5 (Huang e al, 2017)	1854-2019	2° x 2°
Surface wind	Quikscat (Freilich et al., 1994; http://podaac.jpl.nasa.gov database)	2000-2009	0.25° x 0.25°
	CCMP satellite data (Atlas et al., 2011)	1992-2011	0.25° x 0.25°
	ERA5 reanalysis (Hersbach et al., 2020)	1979-2019	0.25° x 0.25°.
	NOAA-20CR v3 reanalysis (Slivinski et al.., 2019)	1836-2015	1° x 1°
Sea surface height	AVISO satellite data (Ducet et al., 2000; www.aviso.altimetry.fr)	1995-2005	0.25° x 0.25°.
	GODAS reanalysis (https://www.esrl.noaa.gov /psd/gridded/data.godas.ht ml)	1980-2020	1° x 1°
Mixed layer depth	de Boyer Montegut 2004	climatology	2° x 2°.

Table 2. Observations and reanalysis datasets selected for this study and specifications of their resolution and coverage period.

Appendix A: Comparison of wind products and offline estimation of stress wind

We compare the wind datasets used in this study by performing a analysis of the wind roses over the CUS region (Fig. A1). To simplify the datasets comparison, we consider one month (August for the IP and MoUS and February for SMUS) when upwelling occurs in these sub-regions. Along the Iberian Peninsula coast (first column) and over the Morocco (second column) to the Senegalese-Mauritanian coast (last column) the trade winds blow from the north-west to north-east approximately 10% to 35% and 15% to 60% of the select time at speeds ranging between 2.5 to 5 m/s and between 5 to 10 m/s respectively. We note a good similarity among wind datasets, across all the considered domains. Quikscat slightly overestimates the wind speed over the SMUS. Therefore, we chose to work with CCMP because it covers a larger period of time than Quikscat. Additionally the agreement between ERA5 and NOAA-20CR-v3 with the observations provide good support for using these reanalysis, exactly matching the present period considered in the climate models (1985-2014).

For all validations data, the wind stress was computed using the bulk formula as Santos et al. (2012) and Sylla et al. (2019):

$$\tau_x = \rho_a C_d (uas^2 + vas^2)^{1/2}) uas \quad and \quad \tau_y = \rho_a C_d (uas^2 + vas^2)^{1/2}) vas \tag{A1}$$

where uas and vas are the zonal and meridional wind components respectively, C_d the drag coefficient (C_d=0.0014 and ρ_a the air density ($\rho_a = 1.22 kg m^{-3}$).
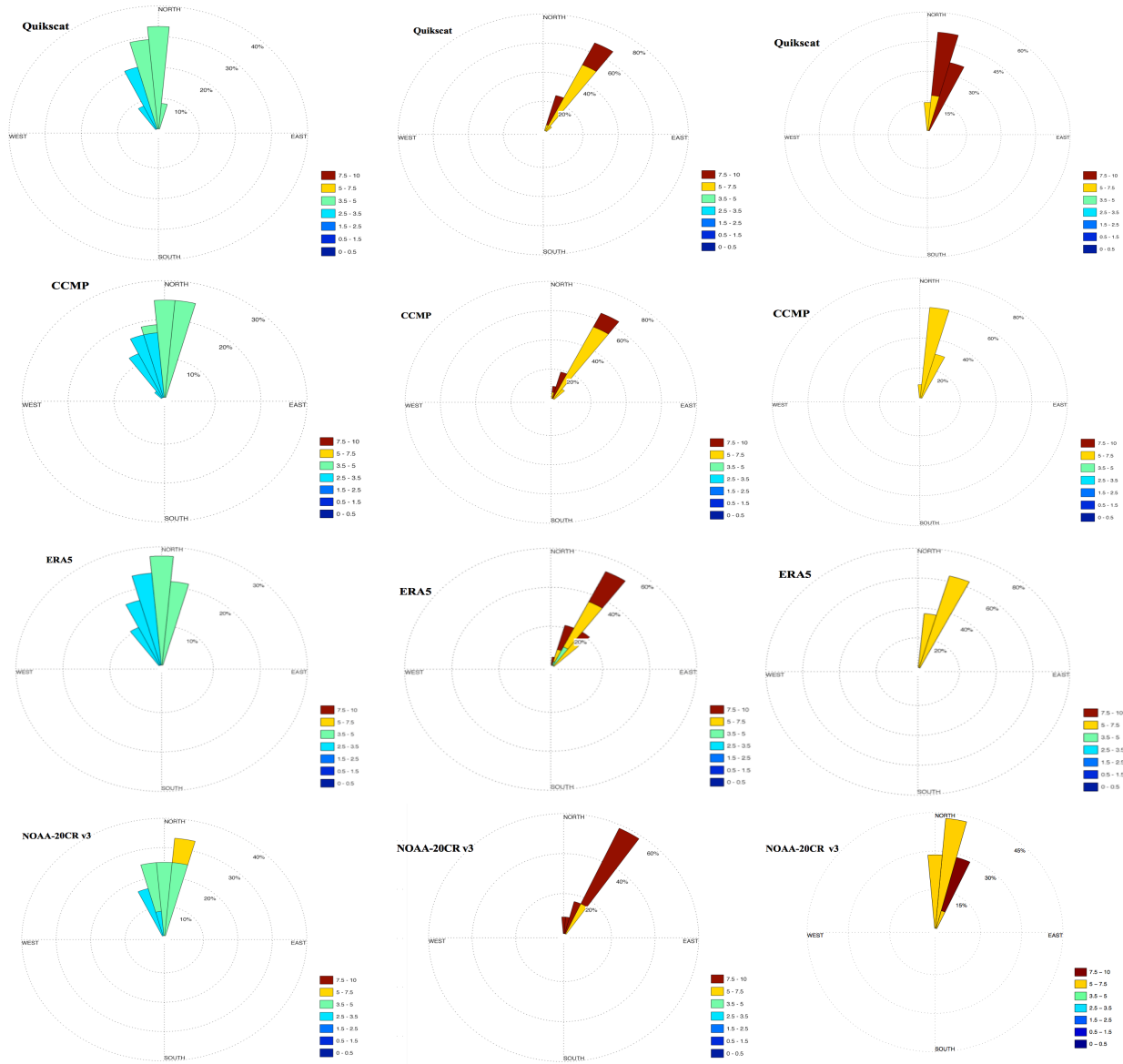
Figure A1. Wind rose diagram in August and averaged over the period [2000-2009] along the Iberian Peninsula (first column) and Morocco (second column) sub-regions and in February along the Senegalo-Mauritanian (last column) from Quikscat, CCMP, ERA5 and NOAA-20CR-v3 wind products. The concentric circles represent a different frequency range, ranging from zero at the center to increasing frequencies at the outer circles. The different colors provide information on the wind speed (in m/s) for each direction.
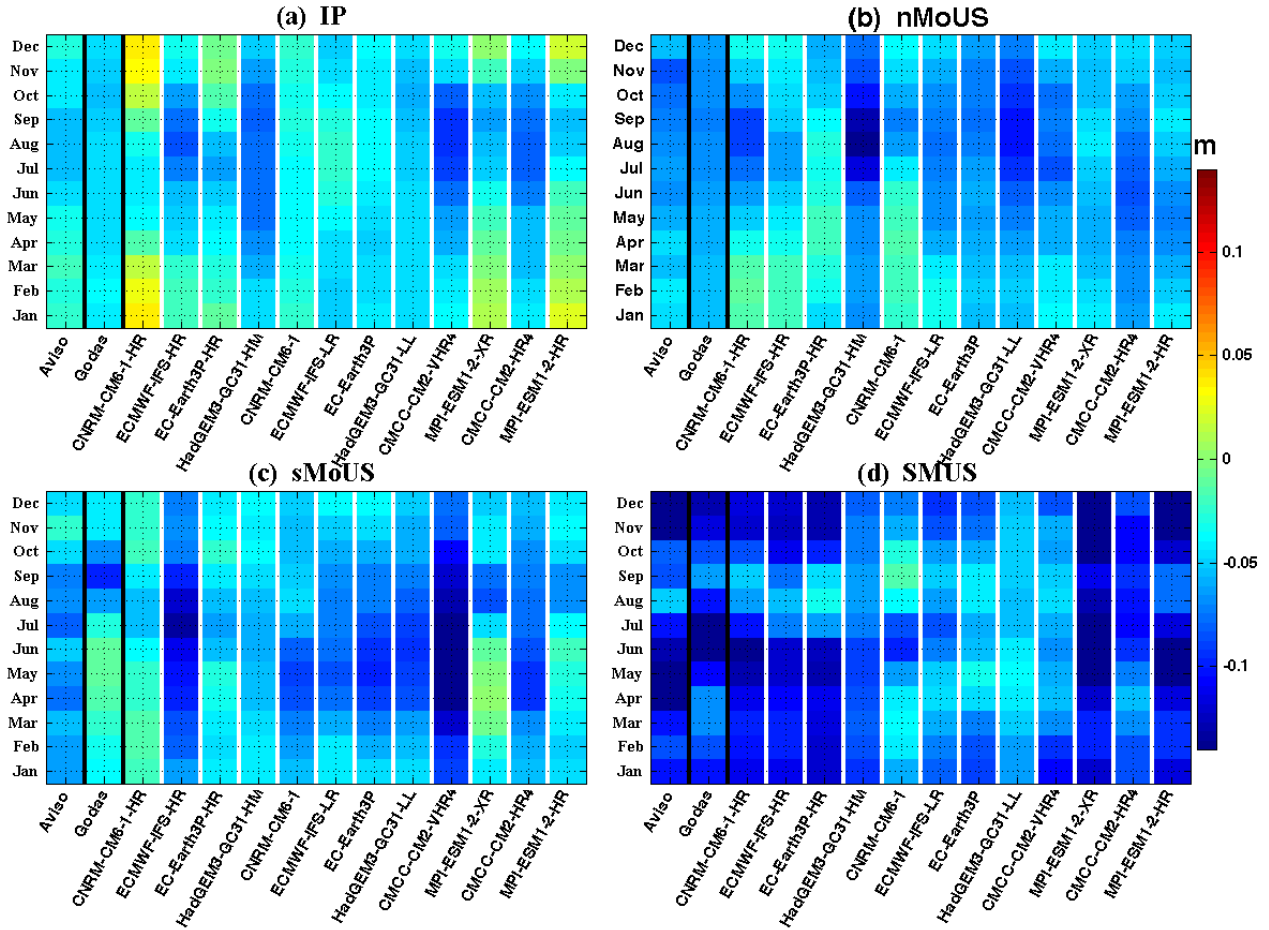
Figure B1. Monthly climatology of the meridional sea surface height difference (units: m) between coastal SSH values at the northernmost and southernmost grid point close to the shore over the Iberian Peninsula (panel a), north and south Morocco sub-domains (panels b and c respectively) and in the Senegalo-Mauritanian sub-region (panel d). The first two columns on the left (highlighted in black) show respectively, the results from AVISO satellite data [1993-2005] and GODAS reanalysis [1985-2014]. The other bands show the individual HighResMIP models.

Appendix C: Comparaison of model skill for different reference datasets
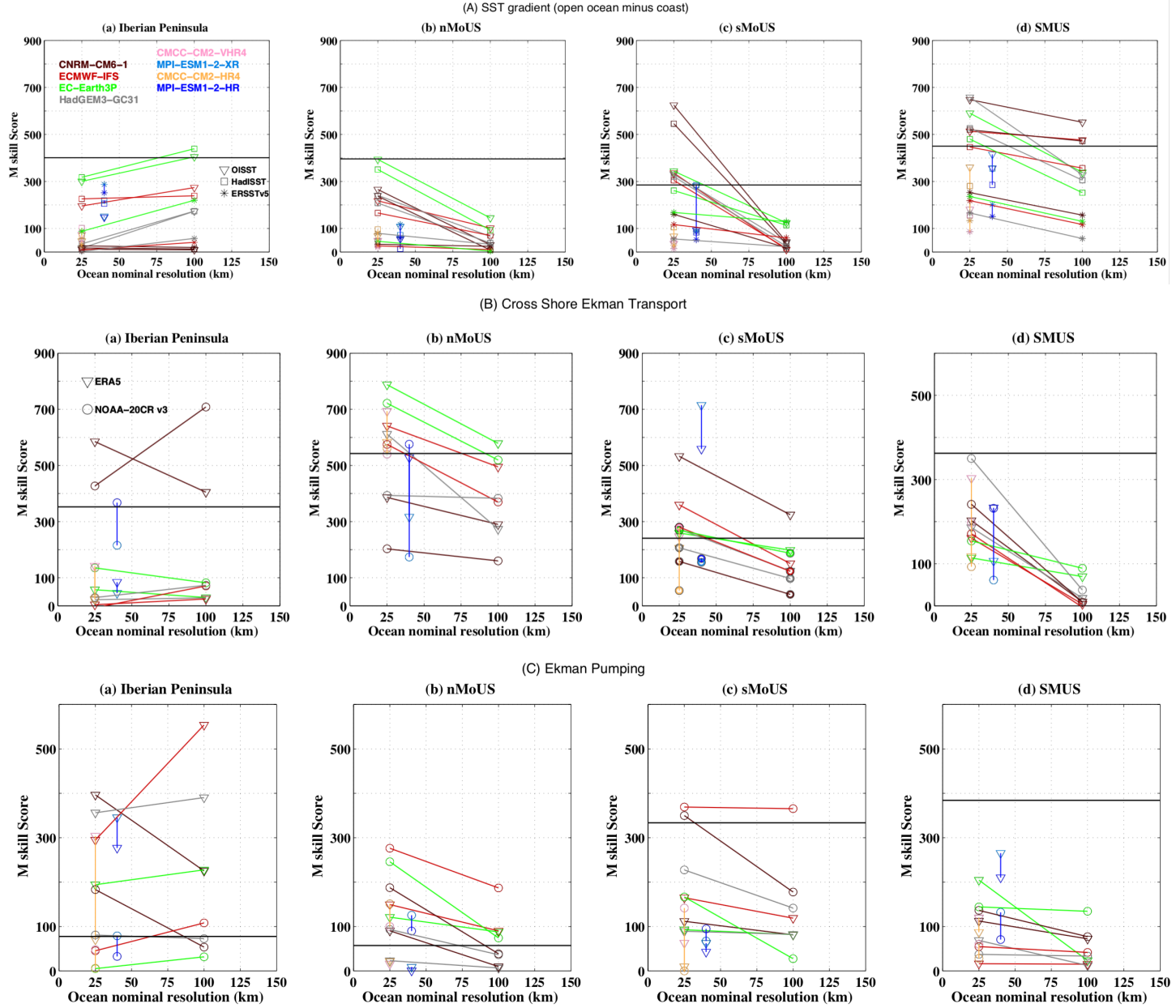
Figure C1. M skill score of upwelling indices as Fig. 6 with each model evaluated to the SSTs datasets (OISST-v2, HadISST and ERSST-v5) for the thermal index and for the dynamical indices to ERA5 and NOAA-20CR-v3.